

Speeding up Local Optimization in Vehicle Routing with Tensor-based GPU Acceleration

Zhenyu Lei ^a, Jin-Kao Hao ^a

^a*LERIA, Université d'Angers, 2 Boulevard Lavoisier, 49045 Angers, France*

Qinghua Wu ^b

^b*School of Management, Huazhong University of Science and Technology, No.1037, Luoyu Road, Wuhan, China*

Abstract

Local search is central to many high-performing metaheuristic algorithms for the vehicle routing problem (VRP) and its variants. However, neighborhood exploration is computationally expensive, especially for large or highly constrained instances. This paper addresses this challenge by proposing an original Tensor-based GPU Acceleration (TGA) framework with two implementations. TGA accelerates move evaluation for common local search operators through an attribute-based solution tensor representation and fully tensorized operator implementations that exploit GPU parallelism. The framework is extensible to a wide range of VRP variants and can be seamlessly integrated into local search-based algorithms. Extensive experiments on three routing problems demonstrate significant advantages over traditional CPU-based implementations. A detailed analysis further reveals performance characteristics, potential bottlenecks, and directions for future improvement.

Keywords: Tensor-based GPU acceleration; Local search; Vehicle routing.

1 Introduction

The Vehicle Routing Problem (VRP) [1,2] is one of the most well-known combinatorial optimization problems and is very computationally challenging due to its NP-hard nature [3]. The VRP involves dispatching a fleet of vehicles to

Email addresses: zhenyu.lei@etud.univ-angers.fr (Zhenyu Lei), jin-kao.hao@univ-angers.fr (Jin-Kao Hao), qinghuawu1005@gmail.com (Qinghua Wu).

serve a set of customers, with each route starting and ending at a depot, while satisfying certain constraints and minimizing the total operational cost. As a fundamental problem in combinatorial optimization, the VRP finds numerous real-world applications in the fields of transportation, logistics, supply chain management, and so on.

Since its introduction, the VRP and its variants have been extensively studied. Methods for solving these problems include exact, approximate, heuristic, and metaheuristic approaches. Due to the high complexity, exact and approximate methods [4–6] are typically limited to small and medium instances, while heuristics and metaheuristics are used for larger instances to obtain good suboptimal solutions efficiently. These include simulated annealing [7,8], tabu search [9,10], genetic algorithms [11,12], and memetic algorithms [13,14], among others. Comprehensive literature reviews on the classification of VRPs and the existing methods can be found in surveys [15–18]. As VRPs grow in size and complexity, computational efficiency remains a challenge, especially with complex constraints. Local search, a key component of high-performing solvers, relies on iterative neighborhood exploration, which is computationally intensive for large or constrained instances. Improving the efficiency of neighborhood evaluation is thus critical for enhancing search performance.

With recent advances in computer hardware, GPU (Graphics Processing Unit) has become increasingly promising for accelerating computationally intensive tasks in combinatorial optimization. With their highly parallel architecture and thousands of cores, GPUs are well suited for large-scale data processing and tasks requiring extensive parallelism, offering significant speedups over traditional CPU-based approaches for solving complex optimization problems. Several studies have explored redesigning classical heuristics and metaheuristics to exploit GPU parallelism. [19] implemented hill climbing and simulated annealing on GPUs and reported substantial speedups, while [20] surveyed GPU-based genetic algorithms across different parallel models and granularities. [21,22] proposed parallel hybrid evolutionary algorithms that exploit algorithmic-level parallelism by running multiple local search processes in parallel within a large population on GPU. [23] developed a GPU-based tabu search for the maximum diversity problem, achieving significant acceleration in neighborhood evaluation.

Recent studies have also explored GPU-based approaches for routing problems, which can be categorized into coarse-grained parallelism, accelerating high-level algorithmic components, and fine-grained parallelism, speeding up neighborhood evaluation in local search. [24] proposed a hybrid genetic algorithm with 2-opt local search for the Capacitated VRP (CVRP) on GPU, parallelizing all algorithmic components. [25] developed a GPU-based multi-objective memetic algorithm for VRPs with route balancing, employing solution-level parallelism and route-level parallelism, though they did not exploit finer

node-level parallelism. [26] achieved significant speedups by parallelizing 2-opt and 3-opt operators for the CVRP. [27] extended GPU-based local search with or-opt, swap, and relocate operators, improving performance but limited to basic travel distance evaluation. [28] proposed a GPU-based variable neighborhood search for VRPs with deliveries and selective pickups, incorporating multiple local search operators, yet primarily optimized travel distance and struggled with complex constraints.

These studies demonstrate the potential of GPU acceleration for solving VRPs, but several limitations remain. Most methods focus on basic VRP variants or simple operators, with limited support for complex constraints and diverse problem settings. Moreover, current approaches rely heavily on low-level CUDA implementations. While powerful, CUDA poses a high barrier to entry due to its steep learning curve and the need for manual management of data transfers, memory layouts, parallel execution, and thread synchronization. This makes widespread adoption challenging, particularly for researchers in operations research without specialized GPU expertise.

To address these gaps, we propose a fine-grained Tensor-based GPU Acceleration (TGA) framework to improve the computational efficiency of local search-based algorithms for complex VRPs. The main contributions are: (1) The TGA framework, along with two implementations, is proposed to accelerate move evaluation by tensorizing local search operators based on an attribute-based solution tensor representation, thereby fully leveraging GPU parallelism. (2) TGA is highly extensible, supporting a wide range of VRP variants and integration into different local search solvers. (3) Unlike CUDA-based approaches, TGA can be implemented using high-level tensor libraries such as PyTorch, substantially lowering the barrier to GPU acceleration for operations research researchers. (4) In-depth theoretical and experimental analyses provide insights into performance characteristics and potential bottlenecks, offering guidance for future research.

To demonstrate its performance and extensibility, we apply TGA to three representative VRPs: CVRP, VRP with Time Windows (VRPTW), and VRP with Simultaneous Pickup and Delivery and Time Windows (VRPSPDTW). Results on benchmark instances confirm that the TGA effectively handles diverse constraints and achieves substantial efficiency gains over traditional CPU-based implementations.

The remainder of this paper is organized as follows. Section 2 formally defines the VRPs. Section 3 presents an overview of GPU architecture and tensor computation, forming the basis of the proposed framework. Section 4 introduces essential background on attribute matrices and sequence concatenation-based move evaluation. Section 5 presents the tensor-based GPU acceleration framework. Section 6 reports computational results on benchmark instances

and provides an in-depth analysis of the framework’s advantages and limitations. Section 7 discusses its extensibility and limitations, while Section 8 concludes the paper. A supplementary document is provided that summarizes the key notations (Section A1), describes the algorithmic framework of the tested algorithms (Section A2), and reports detailed computational results (Sections A3-A4).

2 Problem definition

This section introduces the three typical routing problems that serve as the case studies: the Capacitated VRP, the VRP with Time Windows, and the VRP with Simultaneous Pickup and Delivery and Time Windows. The VRP-SPDTW is a generalization of both the CVRP and the VRPTW. Therefore, we will focus on defining the VRPSPDTW, while showing how it is reduced to these more specific problems.

All three problems can be defined on a complete graph $\mathcal{G} = (\mathcal{V}, \mathcal{E})$, where the vertices or nodes $\mathcal{V} = \{v_0, v_1, \dots, v_{N_C}\}$ represent the depot v_0 and the N_C customers $\{v_1, \dots, v_{N_C}\}$. The edges $\mathcal{E} = \{e_{ij} | v_i, v_j \in \mathcal{V}\}$ represent the connections between these nodes. Each customer node $v_i \in \mathcal{V}$ ($i \neq 0$) is associated with a delivery demand d_i and a pickup demand p_i . This means that the vehicle must deliver d_i units of goods from the depot v_0 to v_i and pick up p_i units from v_i back to the depot. Furthermore, each node v_i has a time window $[e_i, l_i]$ and a service time s_i , which specifies the earliest and latest time for the service, as well as the time spent at node v_i for the service. The depot has a time window $[e_0, l_0]$, specifying the earliest departure and latest return time, with its service time s_0 set to 0. Additionally, the travel distance and travel time matrices, $\mathcal{C} = (c_{ij})$ and $\mathcal{T} = (t_{ij})$, store the travel distance and time for each edge $e_{ij} \in \mathcal{E}$. For the VRPTW and the CVRP, the pickup demand $p_i = 0$. Additionally, the CVRP does not consider time-related attributes such as travel time, service time, or time windows.

A fleet of M homogeneous vehicles, each with a capacity \mathcal{Q} , serves all customers, starting and ending at the depot v_0 , while satisfying various constraints, including capacity and time windows. A solution S is represented as a set of closed routes $S = \{R_1, \dots, R_M\}$, where each route R_i consists of a sequence of nodes $\{n_{i,0}, n_{i,1}, \dots, n_{i,\mathcal{L}_i}, n_{i,\mathcal{L}_i+1}\}$ visited by the i -th vehicle. Here, $n_{i,j}$ denotes the j -th node in route R_i and \mathcal{L}_i is the number of served customers in that route. Thus, the length of route R_i is $|R_i| = \mathcal{L}_i + 2$. Note that both the first and last nodes in route R_i are the depot v_0 (i.e., $n_{i,0} = v_0$ and $n_{i,\mathcal{L}_i+1} = v_0$). To ensure that the load of each vehicle does not exceed its capacity \mathcal{Q} , the condition $q_{n_{i,j}} \leq \mathcal{Q}$ must hold for all $n_{i,j} \in R_i$, where $q_{n_{i,j}}$ represents the load of the i -th vehicle after visiting node $n_{i,j}$. For variants

that incorporate time windows, let $a_{n_{i,j}}$ denote the arrival time at node $n_{i,j}$. Arriving before $e_{n_{i,j}}$ results in a wait time of $w_{n_{i,j}} = \max\{e_{n_{i,j}} - a_{n_{i,j}}, 0\}$, while arriving after $l_{n_{i,j}}$ renders the route infeasible.

$$\begin{aligned} \text{Minimize} \quad & f(S) = \mu_1 \cdot M + \mu_2 \cdot D(S) \\ \text{Subject to} \quad & D(S) = \sum_{i=1}^M \sum_{j=0}^{\mathcal{L}_i} c_{n_{i,j}n_{i,j+1}} \\ & S = \{R_1, \dots, R_M\} \\ & R_i = \{n_{i,0}, n_{i,1}, \dots, n_{i,\mathcal{L}_i}, n_{i,\mathcal{L}_i+1}\}, \quad i = 1, \dots, M \end{aligned} \tag{1}$$

Typically, we can describe the objective function of these problems as minimizing the total cost, which is the weighted sum of the number of vehicles and the travel distance with predefined weights, as shown in Equation (1), where μ_1 and μ_2 represent the costs or weights assigned to the vehicle dispatching and the travel distance, respectively.

3 GPU and tensor computation

This section provides background on GPU architecture, CUDA programming, and tensor computation, forming the basis of our acceleration method.

3.1 GPU architecture

Originally designed for graphics rendering, GPUs are specialized parallel processors that are now widely used for general-purpose computing in scientific simulations, data analytics, and artificial intelligence. Unlike CPUs, which prioritize low-latency execution of sequential instructions through complex control logic and extensive caching, GPUs dedicate most of resources to arithmetic units, enabling thousands of lightweight threads to execute concurrently.

NVIDIA GPUs dominate high-performance and scientific computing due to their performance and mature software ecosystem. The fundamental unit of NVIDIA GPUs, the *Streaming Multiprocessor* (SM), integrates numerous CUDA cores, registers, shared memory, and caches, enabling thousands of threads to cooperate efficiently. Execution on NVIDIA GPUs follows the SIMT (Single Instruction, Multiple Threads) model, where threads are organized into 32-thread *warps* that execute the same instruction on different data, simplifying scheduling and enabling scalable fine-grained parallelism. Additionally, the GPU memory hierarchy supports high-throughput workloads, with large high-latency global memory, fast per-SM shared memory for inter-thread communication, and low-latency per-thread registers.

Table 1

Comparison of NVIDIA GPUs: V100, A100, H100.

GPU	Year	Arch.	SMs	Cores/SM	Total Cores	Memory	Memory Bandwidth	Compute Throughput (TFLOPS)
V100	2017	Volta	80	64	5,120	16/32 GB HBM2	~900-1,134 GB/s	~15.7 (FP32) / ~7.8 (FP64)
A100	2020	Ampere	108	64	6,912	40/80 GB HBM2e	~1.6-2.0 TB/s	~19.5 (FP32) / ~9.7 (FP64)
H100	2022	Hopper	132	128	16,896	80 GB HBM3	~3.0-3.2 TB/s	~67 (FP32) / ~34 (FP64)

Table 1 summarizes three recent NVIDIA GPU generations, showing consistent increases in SMs, CUDA cores, memory capacity, memory bandwidth, and floating-point throughput. More SMs, cores, and higher compute throughput enhance parallelism and speed up compute-intensive workloads. Larger and faster memory supports larger datasets locally, while higher memory bandwidth enables faster data transfer between memory and compute units. Together, these improvements substantially boost modern GPUs’ ability to handle large-scale, complex parallel workloads in scientific and industrial applications.

3.2 CUDA programming

NVIDIA’s Compute Unified Device Architecture (CUDA) is the primary framework for general-purpose GPU programming on NVIDIA hardware. It provides a C/C++ based model in which developers write kernels executed in parallel by many lightweight threads. CUDA exposes hardware concepts such as threads, blocks, warps, and multiple levels of memory, offering fine-grained control over parallel execution and data movement.

Despite its flexibility, CUDA development is challenging. Programmers must explicitly manage device memory, data transfers between CPU and GPU, and thread synchronization. High performance requires deep knowledge of GPU architecture, including how to design coalesced memory accesses, avoid bank conflicts, minimize warp divergence, and tune occupancy. CUDA programming is thus inherently more time-consuming and error-prone than high-level CPU programming, limiting adoption among operations researchers who primarily focus on algorithm design or problem modeling and often lack these specialized skills.

3.3 Tensor computation

In scientific computing and machine learning, tensor computation has emerged as an effective paradigm for exploiting GPU acceleration. A *tensor* is a multi-dimensional array that generalizes scalars (0-D), vectors (1-D), and matrices (2-D) to higher dimensions. On GPUs, tensors are typically stored as contiguous memory blocks, enabling coalesced memory access and efficient parallel

execution. Tensor operations are inherently parallel, as computations on different elements can be distributed across thousands of GPU cores, allowing tensor-based workloads to fully exploit the massive parallelism of modern GPU architectures.

High-level frameworks such as PyTorch and TensorFlow provide a rich set of tensor operations, including element-wise arithmetic, slicing, reshaping, and reduction. These frameworks automatically translate tensor operations into highly optimized GPU kernels, relieving developers from explicitly managing threads, memory transfers, and kernel launches, which are required in low-level CUDA programming. By abstracting away hardware-specific details, tensor computation enables researchers to concentrate on algorithmic design while still achieving high-performance execution.

Thus, in this study, we model the solution with tensor representation, and implement move evaluation of local search operators using tensor operations. This design enables efficient exploitation of GPU parallelism through high-level tensor frameworks, making GPU acceleration more accessible and practical for researchers in operations research.

4 Move evaluation and attribute matrix

Efficient move evaluation is a critical step in the search process of local search algorithms and directly affects both solution quality and search efficiency. Our proposed tensor-based GPU acceleration (TGA) framework builds upon a constant-time move evaluation method [29–31]. Although this method has not been explicitly named in prior works, we refer to it in this paper as *sequence concatenation-based move evaluation*.

4.1 Sequence concatenation-based move evaluation

Sequence concatenation-based move evaluation conceptualizes common local search move operators, such as *Relocate*, *Swap*, *2-opt**, and *2-opt*, as the concatenation of multiple route subsequences. This allows for efficient neighborhood evaluations with respect to both the objective function and the associated constraints.

The *Relocate* operator moves a sequence of nodes to a new position within the same route or a different route, while the *Swap* operator exchanges two sequences of nodes. The *2-opt** operator, applied between two routes, breaks one edge in each route, exchanges the subsequences, and reconnects them to

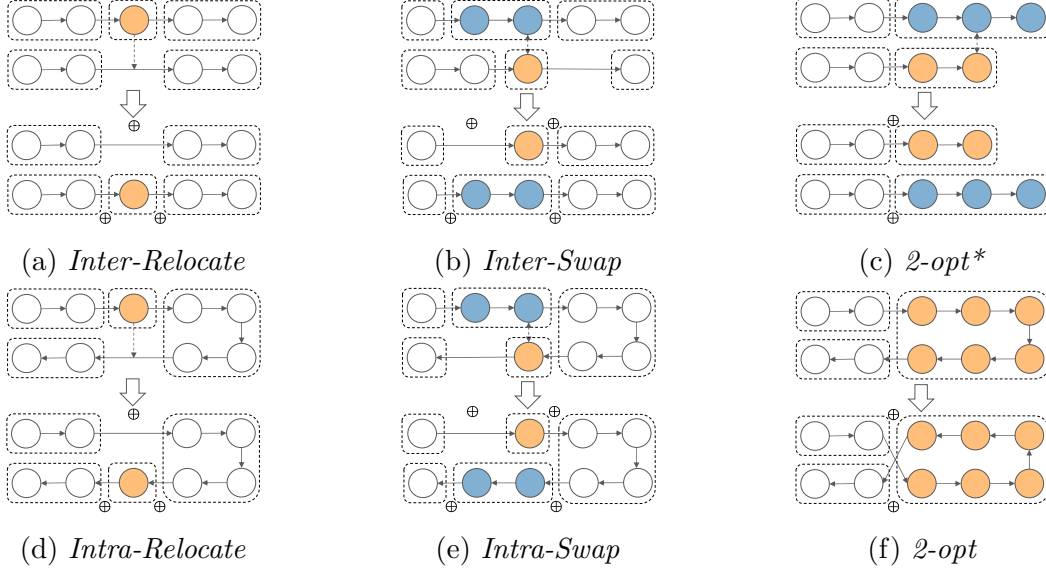


Fig. 1. Illustration of operators and their concatenation operations. Dotted boxes represent the route subsequences. Symbols \oplus denote the concatenation operations.

form new routes. In contrast, the *2-opt* move operates within a single route by breaking two non-adjacent edges and reconnecting the reversed subsequence. Note that *2-opt* is only suitable for problems with symmetric distance matrices and without directed constraints, such as time windows. Based on whether the operators act within a single route or between two routes, these operators can be classified into two categories: *intra-route* operators, which act within a single route (*Intra-Relocate*, *Intra-Swap* and *2-opt*), and *inter-route* operators, which operate between two routes (*Inter-Relocate*, *Inter-Swap*, and *2-opt**). Figure 1 illustrates the concatenation operations for each operator. The concatenation operations can also be extended to other routing operators with similar characteristics, such as 3-opt, Or-opt, and Cross-exchange.

4.2 Attribute matrices

To enable efficient sequence concatenation-based move evaluation, we introduce *attribute matrices*, which store the attribute values of all feasible route subsequences. These values are precomputed during the update stage, enabling constant-time computation of concatenated sequences in the move evaluation stage. Specifically, for each route and for each relevant attribute, an *attribute matrix* is constructed to record the attribute values of all feasible subsequences. Figure 2 illustrates a route of length $|R| = 5$ along with its attribute matrix, where a_{ij} denotes the attribute value associated with the subsequence from the i -th node to the j -th node of the route. For example, for the travel distance attribute, a_{ij} corresponds to the cumulative travel distance between the i -th and j -th nodes. Note that only the upper triangular portion

of the matrix contains valid entries. These attributes are tailored to specific problem settings and constraints, providing strong adaptability across various VRP variants.

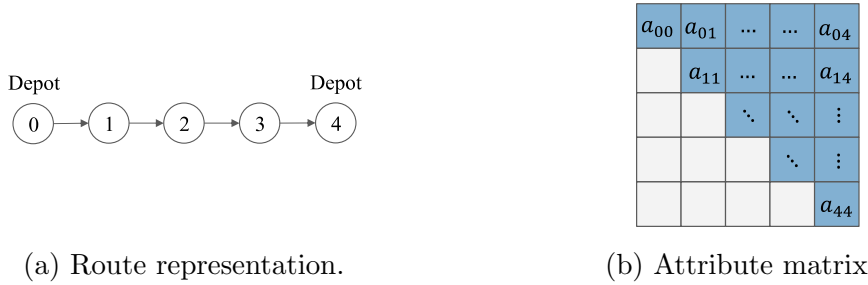


Fig. 2. Illustration of a route of length $|R| = 5$ and its corresponding attribute matrix. The first (0) and last (4) nodes represent the depot.

Building upon these attribute matrices, constant-time move evaluation is achieved through sequence concatenation operations, which constitute a core component of the proposed tensor-based GPU acceleration framework.

4.3 Calculations of concatenation operations

This section details the calculations of concatenation operations using attribute matrices. We focus on commonly used attributes: *travel distance*, *load related attributes*, and *time window related attributes*, which are sufficient for the studied VRPs (CVRP, VRPTW, and VRPSPDTW) and widely adopted in vehicle routing. This concatenation operation can be extended to attributes required by other VRP variants, such as cumulative distance, load-dependent cost as discussed in [29].

Let σ denote a route subsequence. A single-node subsequence is denoted by $\sigma^0 = \{v_k\}$, while $\sigma_1 = \{v_i, \dots, v_j\}$ and $\sigma_2 = \{v_k, \dots, v_l\}$ represent two generic subsequences. The concatenation of σ_1 and σ_2 is denoted by $\sigma_1 \oplus \sigma_2$. The following subsections describe how attributes are updated under concatenation.

4.3.1 Travel distance

Travel distance is a fundamental attribute in routing problems. Let $D(\sigma)$ denote the travel distance of a subsequence σ . For a single-node subsequence σ^0 and the concatenation of two route subsequences σ_1 and σ_2 , the travel

distance is computed as follows.

$$D(\sigma^0) = 0 \quad (2a)$$

$$D(\sigma_1 \oplus \sigma_2) = D(\sigma_1) + c_{jk} + D(\sigma_2) \quad (2b)$$

where c_{jk} denotes the travel distance between the last node v_j of σ_1 and the first node v_k of σ_2 .

4.3.2 Load and capacity

To evaluate load and capacity constraints, we maintain three load-related attributes for each route subsequence σ : the incoming load $L_I(\sigma)$, the outgoing load $L_O(\sigma)$, and the maximum load $L_M(\sigma)$. The computation of these attributes is defined as follows.

$$L_I(\sigma^0) = d_k, \quad L_O(\sigma^0) = p_k, \quad L_M(\sigma^0) = \max\{d_k, p_k\} \quad (3a)$$

$$L_I(\sigma_1 \oplus \sigma_2) = L_I(\sigma_1) + L_I(\sigma_2) \quad (3b)$$

$$L_O(\sigma_1 \oplus \sigma_2) = L_O(\sigma_1) + L_O(\sigma_2) \quad (3c)$$

$$L_M(\sigma_1 \oplus \sigma_2) = \max\{L_M(\sigma_1) + L_I(\sigma_2), L_O(\sigma_1) + L_M(\sigma_2)\} \quad (3d)$$

For CVRP and VRPTW, where pickup demands are zero ($p_k = 0$), the formulation simplifies and only the maximum load needs to be maintained:

$$L_M(\sigma^0) = d_k \quad (4a)$$

$$L_M(\sigma_1 \oplus \sigma_2) = L_M(\sigma_1) + L_M(\sigma_2) \quad (4b)$$

4.3.3 Time windows

Time window constraints can be handled using the time-warp technique [32,33], which allows the evaluation of time window violations within subsequences. Each subsequence σ maintains the earliest and latest arrival times ($T_E(\sigma)$ and $T_L(\sigma)$), duration $T_D(\sigma)$, and time window violation $T_V(\sigma)$. Let t_{jk} denote the travel time between the last node of σ_1 and the first node of σ_2 . The concatenation rules are given by:

$$T_D(\sigma^0) = s_k, \quad T_E(\sigma^0) = e_k, \quad T_L(\sigma^0) = l_k, \quad T_V(\sigma^0) = 0 \quad (5a)$$

$$\Delta_t = T_D(\sigma_1) + T_W(\sigma_1) + t_{jk} - T_V(\sigma_1) \quad (5b)$$

$$\Delta_w = \max\{T_E(\sigma_2) - \Delta_t - T_L(\sigma_1), 0\} \quad (5c)$$

$$\Delta_v = \max\{T_E(\sigma_1) + \Delta_t - T_L(\sigma_2), 0\} \quad (5d)$$

$$T_D(\sigma_1 \oplus \sigma_2) = T_D(\sigma_1) + t_{jk} + \Delta_w + T_D(\sigma_2) \quad (5e)$$

$$T_E(\sigma_1 \oplus \sigma_2) = \max\{T_E(\sigma_1), T_E(\sigma_2) - \Delta_t\} - \Delta_w \quad (5f)$$

$$T_L(\sigma_1 \oplus \sigma_2) = \min\{T_L(\sigma_1), T_L(\sigma_2) - \Delta_t\} + \Delta_v \quad (5g)$$

$$T_V(\sigma_1 \oplus \sigma_2) = T_V(\sigma_1) + \Delta_v + T_V(\sigma_2) \quad (5h)$$

By maintaining the attribute matrices, all concatenation operations can be computed in constant time, enabling efficient evaluation of attribute differences between the current solution and its neighbors within local search neighborhoods.

5 Tensor-based GPU acceleration for local search operators

In this section, we present the Tensor-based GPU Acceleration (TGA) framework, which is designed to improve computational efficiency of commonly used local search operators in vehicle routing problems. The core lies in the design of the attribute-based solution tensor representation, and the tensor-based implementation of local search operators. By extracting and concatenating the relevant attribute tensors from the solution tensor representation, we can efficiently implement the sequence concatenation-based move evaluation with the help of GPU parallelism.

5.1 Workflow of the TGA framework between CPU and GPU

The proposed TGA framework is designed with a low degree of coupling between the CPU and the GPU. The computationally intensive move evaluation of local search operators is entirely offloaded to the GPU. Meanwhile, the CPU handles only the updates based on the GPU’s computation results. This design ensures that the TGA can be easily integrated into a wide range of local search-based algorithms and frameworks.

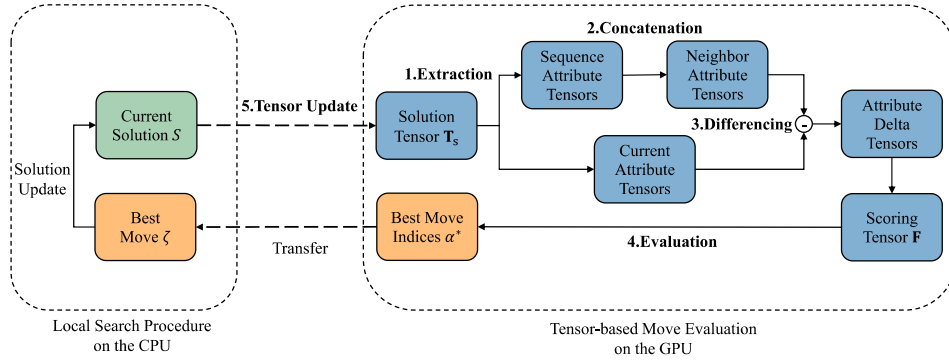


Fig. 3. Workflow of the TGA framework.

The workflow of the TGA framework is illustrated in Figure 3. For a given solution S to be improved by local search on the CPU, a solution tensor \mathbf{T}_s is first initialized on the GPU using the attribute matrices derived from S . Tensor-based move evaluation is then performed on the GPU using \mathbf{T}_s . To

fully exploit GPU parallelism, the best-improvement strategy is employed to select the best move among all candidate moves.

The tensor-based implementation of each operator follows a generic five-step process, the first four steps perform tensor-based move evaluation, and the final step performs the necessary updates. Specifically, these steps are: (1) **Extraction**: Extract relevant *sequence attribute tensors* from the solution tensor \mathbf{T}_s according to the specific operator. (2) **Concatenation**: Concatenate the extracted attribute tensors to construct the *neighbor attribute tensors* which represent all neighboring solutions within the operator’s neighborhood. (3) **Differencing**: Compute the *attribute delta tensors* containing the differences between the current and modified routes. (4) **Evaluation**: Compute the *scoring tensor* \mathbf{F} based on the evaluation function and identify the best-improvement value and the corresponding indices α^* in \mathbf{F} for the best move ζ . (5) **Update**: Transfer the best move back to the CPU, update the solution S , and synchronize the updated solution tensor \mathbf{T}_s along with other auxiliary tensors on the GPU for the next iteration.

5.2 Attribute-based solution tensor representation

As described in Section 4.2, we use *attribute matrices* to store attribute values, enabling constant-time move evaluation. Building on this, we aggregate these attribute matrices into a solution tensor \mathbf{T}_s for GPU acceleration. Formally, the solution tensor \mathbf{T}_s is a 4-dimensional tensor defined as

$$\mathbf{T}_s \in \mathbb{R}^{I \times J \times K \times K} \quad (6)$$

Here, I denotes the number of maintained attributes, J the maximum number of routes, and $K = \max_{1 \leq i \leq M} \{|R_i|\}$ the maximum route length, i.e., the number of nodes in the longest route. The entries of \mathbf{T}_s are indexed as

$$(\mathbf{T}_s)_{ijkl}, \quad i \in \{1, \dots, I\}, j \in \{1, \dots, J\}, k, l \in \{1, \dots, K\} \quad (7)$$

where $(\mathbf{T}_s)_{ijkl}$ represents the value of the i -th attribute for the subsequence starting at position k and ending at position l in the j -th route. Figure 4 illustrates the structure of the solution tensor representation.

To handle considered attributes introduced in Section 4.3, we maintain the corresponding key attribute tensors: travel distance (\mathbf{D}), duration (\mathbf{T}_D), earliest and latest arrival times ($\mathbf{T}_E, \mathbf{T}_L$), time window violations (\mathbf{T}_V), incoming and outgoing loads ($\mathbf{L}_I, \mathbf{L}_O$), and maximum load (\mathbf{L}_M). Auxiliary tensors are also introduced to support efficient computation, including the first and last node indices of each sequence ($\mathbf{I}_S, \mathbf{I}_E$) and a boolean mask (\mathbf{B}) for valid entries. This attribute-based representation is flexible and can be extended for other VRP variants.

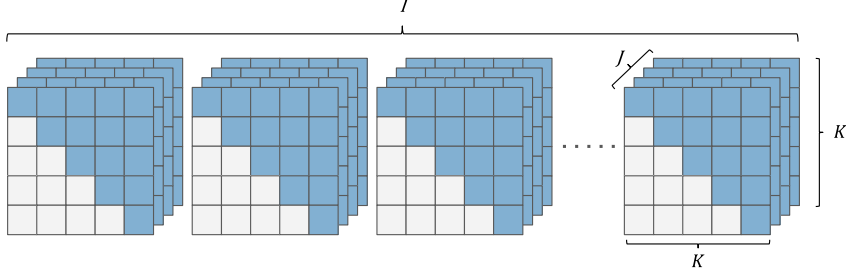


Fig. 4. Illustration of the solution tensor representation.

5.3 Tensor-based implementation of local search operators

Building on the solution tensor \mathbf{T}_s defined in Equation (7), we develop the tensor-based implementation for four common local search operators in vehicle routing, *Relocate*, *Swap*, *2-opt**, and *2-opt*, as introduced in Section 4.1, taking advantage of GPU parallelism to speed up move evaluation. The following sections describe the five generic steps of the tensor-based implementation in detail.

5.3.1 Extraction

Based on the sequence concatenation-based move evaluation introduced in Section 4, *Extraction* step extracts specific parts of the solution tensor \mathbf{T}_s , referred to as *sequence attribute tensors*, using tensor operations such as indexing, slicing, and reshaping. These tensors contain all attribute values associated with the relevant route subsequences which are required to compute the attributes of the concatenated sequences in subsequent steps. This process leverages highly parallelizable tensor operations, such as slicing, indexing, and reshaping, making it well-suited for GPU acceleration. The *Extraction* step is the critical step that distinguishes the operators and is implemented separately for *intra-route* and *inter-route* operators.

5.3.1.1 Route-based extraction for intra-route operators We propose a *route-based extraction* for the intra-route operators (*Intra-Relocate*, *Intra-Swap* and *2-opt*), which involve only a single route.

As shown in Figure 1f, the *2-opt* operator divides the route at two cut points into three subsequences: the head sequence S_h , the middle sequence S_m , and the tail sequence S_t . The head sequence contains the nodes before the first cut, the middle sequence contains the nodes between the two cuts, and the tail sequence contains the nodes after the second cut. In the solution tensor \mathbf{T}_s , we extract the attribute values of all subsequences fully contained in each of these three parts into three *sequence attribute tensors* \mathbf{S}_h , \mathbf{S}_m , and \mathbf{S}_t . Formally, for

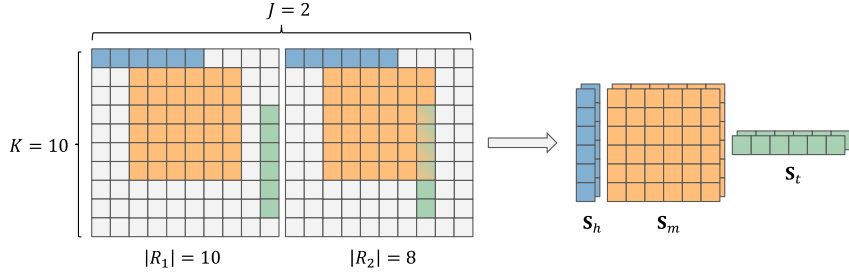


Fig. 5. Example of the extraction operation for 2-opt . For clarity, we illustrate a single-attribute slice of the solution tensor and show a 3D tensor with dimensions $J \times K \times K = 2 \times 10 \times 10$, omitting the first dimension of \mathbf{T}_s .

each attribute $i \in \{1, \dots, I\}$ and route $j \in \{1, \dots, J\}$, we define:

$$\mathbf{S}_h = (\mathbf{T}_s)_{ij1l}, \quad l \in \{1, \dots, K-4\} \quad (8a)$$

$$\mathbf{S}_m = (\mathbf{T}_s)_{ijkl}, \quad k \in \{2, \dots, K-3\}, l \in \{3, \dots, K-2\} \quad (8b)$$

$$\mathbf{S}_t = (\mathbf{T}_s)_{ijk|R_j|}, \quad k \in \{4, \dots, K-1\} \quad (8c)$$

As illustrated in Figure 5, for each attribute i and route R_j , the head sequence tensor \mathbf{S}_h is always located in the first row of the attribute matrix, capturing the attribute values of relevant subsequences from the first node ($k=1$) up to the first cut point. The middle sequence tensor \mathbf{S}_m stores attributes between two cut points, forming a square submatrix. The tail sequence tensor \mathbf{S}_t stores attributes from second cut point to the last node, corresponding to the R_j -th column of the attribute matrix. The similar principles of the extraction process are illustrated for the other operators in the subsequent Figures 6-9. Since the 2-opt operator is only applied to VRP variants with symmetric settings, reversing the middle sequence can be implemented by swapping the first node index tensor \mathbf{I}_s and the last node index tensor \mathbf{I}_e of the attribute tensor \mathbf{S}_m . The reshaping operation is consistently applied to extracted *sequence attribute tensors* across all operators, enabling the subsequent *Concatenation* step via tensor broadcasting.

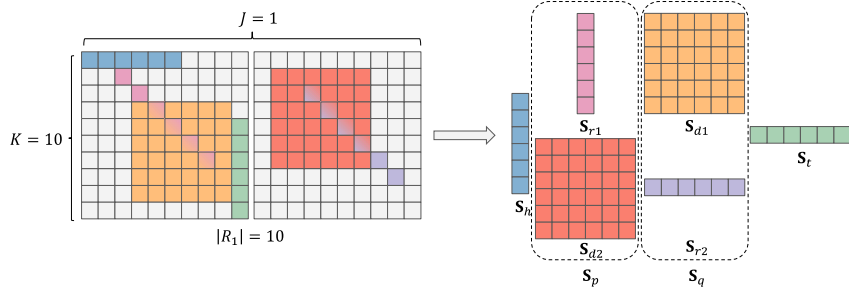


Fig. 6. Example of the extraction operation for *Intra-Relocate*. For clarity, we illustrate a single-attribute slice of the solution tensor and show a 3D tensor with dimensions $J \times K \times K = 1 \times 10 \times 10$, omitting the first dimension of \mathbf{T}_s and setting $J=1$.

As shown in Figure 1d, the *Intra-Relocate* operator divides a route into four

subsequences: the head sequence S_h , the relocated sequence S_r of length N ($N > 0$), the destination sequence S_d preceding the insertion position, and the tail sequence S_t . The relative order of S_r and S_d depends on whether the relocated sequence is moved forward or backward along the route. To handle both cases efficiently on the GPU, we construct two combined sequence attribute tensors, \mathbf{S}_p and \mathbf{S}_q . For each attribute $i \in \{1, \dots, I\}$ and route $j \in \{1, \dots, J\}$, the extraction proceeds as follows:

$$\mathbf{S}_h = (\mathbf{T}_s)_{ij1l}, \quad l \in \{1, \dots, K - N - 2\} \quad (9a)$$

$$\mathbf{S}_t = (\mathbf{T}_s)_{ijk|R_j|}, \quad k \in \{N + 3, \dots, K\} \quad (9b)$$

$$\mathbf{S}_p = \text{concat}(\mathbf{S}_{r1}, \mathbf{S}_{d2}), \quad \mathbf{S}_q = \text{concat}(\mathbf{S}_{d1}, \mathbf{S}_{r2}) \quad (9c)$$

The auxiliary tensors \mathbf{S}_{r1} , \mathbf{S}_{r2} , \mathbf{S}_{d1} , and \mathbf{S}_{d2} capture the two possible relative positions of the relocated and destination sequences along the route. Specifically, \mathbf{S}_{r1} and \mathbf{S}_{d1} correspond to the case where the relocated sequence S_r precedes the destination sequence S_d , while \mathbf{S}_{r2} and \mathbf{S}_{d2} correspond to the opposite case. These tensors are defined as follows.

$$\mathbf{S}_{r1} = (\mathbf{T}_s)_{ijk(k+N-1)}, \quad k \in \{2, \dots, K - N - 1\} \quad (10a)$$

$$\mathbf{S}_{d2} = (\mathbf{T}_s)_{ijkl}, \quad k, l \in \{2, \dots, K - N - 1\} \quad (10b)$$

$$\mathbf{S}_{d1} = (\mathbf{T}_s)_{ijkl}, \quad k, l \in \{N + 2, \dots, K - 1\} \quad (10c)$$

$$\mathbf{S}_{r2} = (\mathbf{T}_s)_{ijk(k+N-1)}, \quad k \in \{3, \dots, K - N\} \quad (10d)$$

Similarly, as illustrated in Figure 1e, the *Intra-Swap* operator divides a single

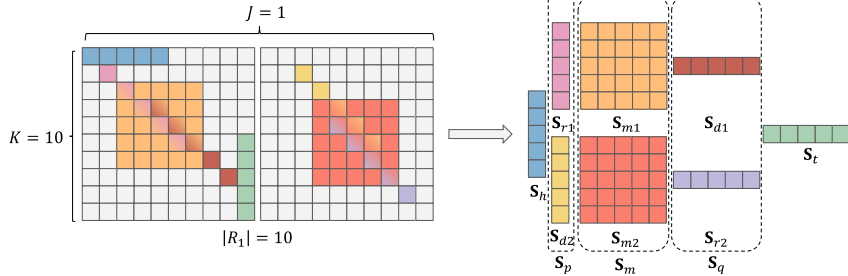


Fig. 7. Example of the extraction operation for *Intra-Swap* with $N_1 = 1, N_2 = 2$. For clarity, we illustrate a single-attribute slice of the solution tensor and show a 3D tensor with dimensions $J \times K \times K = 1 \times 10 \times 10$, omitting the first dimension of \mathbf{T}_s and setting $J = 1$.

route into five subsequences: the head sequence S_h , the swapped sequence S_r of length N_1 ($N_1 > 0$), the middle sequence S_m , the swapped sequence S_d of length N_2 ($N_2 > 0$), and the tail sequence S_t . When the two swapped sequences have different lengths ($N_1 \neq N_2$), two cases must be considered, depending on whether S_r or S_d appears first. Thus, we also introduce auxiliary tensors to capture these cases. For each attribute $i \in \{1, \dots, I\}$ and route $j \in \{1, \dots, J\}$,

the extraction process is defined as follows:

$$\mathbf{S}_h = (\mathbf{T}_s)_{ijl}, \quad l \in \{1, \dots, K - N_1 - N_2 - 2\} \quad (11a)$$

$$\mathbf{S}_t = (\mathbf{T}_s)_{ijk|R_j|}, \quad k \in \{N_1 + N_2 + 3, \dots, K\}, \quad (11b)$$

$$\mathbf{S}_p = \text{concat}(\mathbf{S}_{r1}, \mathbf{S}_{d2}), \quad \mathbf{S}_m = \text{concat}(\mathbf{S}_{m1}, \mathbf{S}_{m2}), \quad \mathbf{S}_q = \text{concat}(\mathbf{S}_{d1}, \mathbf{S}_{r2}) \quad (11c)$$

The auxiliary tensors \mathbf{S}_{r1} , \mathbf{S}_{r2} , \mathbf{S}_{m1} , \mathbf{S}_{m2} , \mathbf{S}_{d1} , and \mathbf{S}_{d2} are defined as follows. Here, \mathbf{S}_{r1} , \mathbf{S}_{m1} and \mathbf{S}_{d1} correspond to the case where the swapped sequence S_r precedes the swapped sequence S_d , while \mathbf{S}_{r2} , \mathbf{S}_{m2} and \mathbf{S}_{d2} correspond to the opposite case.

$$\mathbf{S}_{r1} = (\mathbf{T}_s)_{ijk(k+N_1-1)}, \quad k \in \{2, \dots, K - N_1 - N_2 - 1\} \quad (12a)$$

$$\mathbf{S}_{d2} = (\mathbf{T}_s)_{ijk(k+N_2-1)}, \quad k \in \{2, \dots, K - N_1 - N_2 - 1\} \quad (12b)$$

$$\mathbf{S}_{m1} = (\mathbf{T}_s)_{ijkl}, \quad k, l \in \{N_1 + 2, \dots, K - N_2 - 1\} \quad (12c)$$

$$\mathbf{S}_{m2} = (\mathbf{T}_s)_{ijkl}, \quad k, l \in \{N_2 + 2, \dots, K - N_1 - 1\} \quad (12d)$$

$$\mathbf{S}_{d1} = (\mathbf{T}_s)_{ijk(k+N_2-1)}, \quad k \in \{N_1 + 3, \dots, K - N_2\} \quad (12e)$$

$$\mathbf{S}_{r2} = (\mathbf{T}_s)_{ijk(k+N_1-1)}, \quad k \in \{N_2 + 3, \dots, K - N_1\} \quad (12f)$$

5.3.1.2 Route-based extraction for inter-route operators Inter-route operators (*Inter-Relocate*, *Inter-Swap*, and *2-opt**) involve two distinct routes and share a common extraction scheme implemented via the $\mathcal{3}\text{-Seq}(N)$ operation, which splits the route into three subsequences: a head sequence S_h , a middle sequence S_m of length N to be relocated or swapped, and a tail sequence S_t . All three inter-route operators involve two $\mathcal{3}\text{-Seq}$ operations, denoted as $\mathcal{3}\text{-Seq}(N_1)$ and $\mathcal{3}\text{-Seq}(N_2)$. Specifically, for *Inter-Relocate*, $N_1 > 0$ and $N_2 = 0$; for *Inter-Swap*, $N_1 > 0$ and $N_2 > 0$; and for *2-opt**, $N_1 = N_2 = 0$.

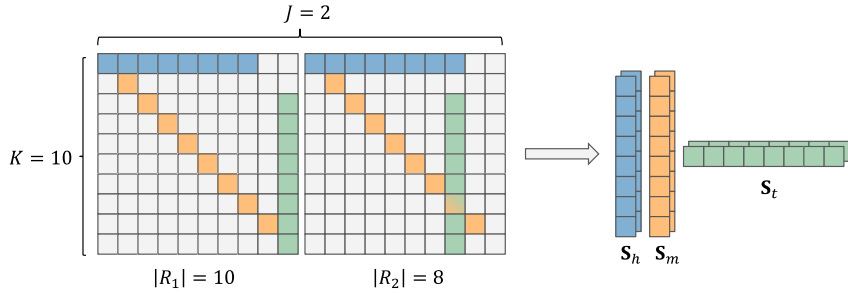


Fig. 8. Example of the route-based $\mathcal{3}\text{-Seq}$ operation with $N = 1$ for inter-route operators. For clarity, we illustrate a single-attribute slice of the solution tensor and show a 3D tensor with dimensions $J \times K \times K = 2 \times 10 \times 10$. Note that the length of the routes affects the tail sequence \mathbf{S}_t .

Building on the same principles used for intra-route operators, we extend the route-based extraction implementation to $\mathcal{3}\text{-Seq}$ operation. For each attribute

$i \in \{1, \dots, I\}$ and route $j \in \{1, \dots, J\}$, the route-based $\mathcal{3}\text{-Seq}(N)$ operation is defined as follows:

$$\mathbf{S}_h = (\mathbf{T}_s)_{ij1l}, \quad l \in \{1, \dots, K - N - 1\}, N \geq 0 \quad (13a)$$

$$\mathbf{S}_m = (\mathbf{T}_s)_{ijk(k+N-1)}, \quad k \in \{2, \dots, K - N\}, \text{ for } N > 0; \quad \emptyset \text{ for } N = 0. \quad (13b)$$

$$\mathbf{S}_t = (\mathbf{T}_s)_{ijk|R_j|}, \quad k \in \{N + 2, \dots, K\}, N \geq 0 \quad (13c)$$

Let L denote the feasible length of the *sequence attribute tensors* after route-based extraction, with $L = K - N - 2$ for the route-based $\mathcal{3}\text{-Seq}$ operation. Notably, this implementation generates high-dimensional intermediate and scoring tensors of size $O(J^2L^2)$ that contain many invalid elements, resulting in substantial memory overhead and increased computational cost in subsequent computations. A detailed complexity analysis is provided in Section 5.4.

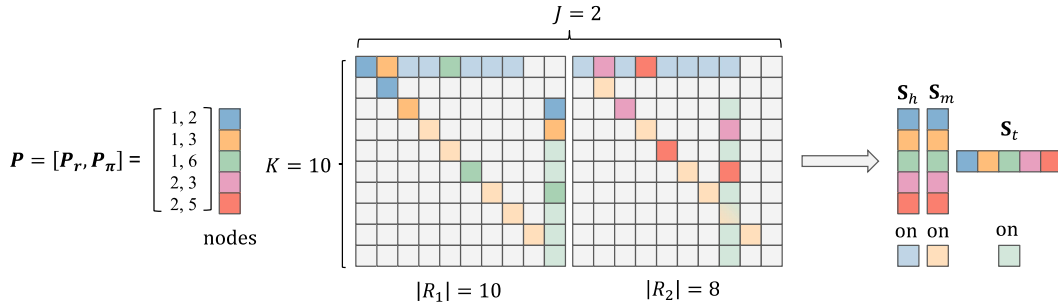


Fig. 9. Example of the node-based $\mathcal{3}\text{-Seq}$ operation. To illustrate the differences between node-based and route-based implementations, we reuse the same setting as in Figure 8. In this example, five nodes are distributed across two routes: the 2nd, 3rd, and 6th nodes on route R_1 , and the 3rd and 5th nodes on route R_2 . The figure shows how the head, middle, and tail sequences are extracted based on node positions, and highlights their relationship to those obtained through the route-based implementation.

5.3.1.3 Node-based extraction for inter-route operators To address the inefficiencies of route-based extraction for inter-route operators, we propose a node-based implementation of the $\mathcal{3}\text{-Seq}$ operation. This approach leverages explicit positional information to extract valid subsequences directly at the node level. Specifically, we construct *positional tensors* $\mathbf{P} = \{\mathbf{P}_r, \mathbf{P}_\pi\}$ from the solution tensor \mathbf{T}_s , which encode the position of each valid node, including depots and customers. The *route index tensor* \mathbf{P}_r identifies the route to which each node belongs, while the *position index tensor* \mathbf{P}_π specifies the node's position within its route. Both \mathbf{P}_r and \mathbf{P}_π are one-dimensional tensors of size Q , where $Q = M + N_C$ denotes the total number of valid nodes across

all routes.

$$\mathbf{S}_h = (\mathbf{T}_s)_{i(p_r)k(p_\pi-1)} \quad (14a)$$

$$\mathbf{S}_m = (\mathbf{T}_s)_{i(p_r)(p_\pi)(p_\pi+N-1)} \quad (14b)$$

$$\mathbf{S}_t = (\mathbf{T}_s)_{i(p_r)(p_\pi+N)|R_{p_r}|} \quad (14c)$$

Using this positional information, we extract the *sequence attribute tensors* \mathbf{S}_h , \mathbf{S}_m , and \mathbf{S}_t only for valid nodes, avoiding the invalid entries generated by the route-based extraction. Given positional indices $p_r \in \mathbf{P}_r$ and $p_\pi \in \mathbf{P}_\pi$, for each attribute $i \in \{1, \dots, I\}$, the node-based extraction distinguishes two cases. If $N > 0$, the middle sequence exists (Equation (14)); if $N = 0$, the middle sequence is empty (Equation (15)).

$$\mathbf{S}_h = (\mathbf{T}_s)_{i(p_r)k(p_\pi)} \quad (15a)$$

$$\mathbf{S}_m = \emptyset \quad (15b)$$

$$\mathbf{S}_t = (\mathbf{T}_s)_{i(p_r)(p_\pi+1)|R_{p_r}|} \quad (15c)$$

Unlike the route-based extraction, which is based on the route structure and produces high-dimensional tensors with many invalid elements, the node-based extraction focuses on valid nodes using their positional information, resulting in greater computational efficiency. As a result, the intermediate and scoring tensors are reduced to size $O(Q^2)$, significantly lowering memory consumption and computational cost and enabling a more efficient GPU implementation.

5.3.1.4 Edge-based extraction for inter-route operators Although the node-based extraction significantly reduces memory usage and computational complexity compared to the route-based method, it still evaluates the entire neighborhood and therefore cannot directly leverage neighborhood reduction strategies [33] commonly used in CPU-based local search, which restrict neighborhood evaluation to promising moves based on specific criteria to improve search efficiency. To overcome this limitation, we propose an edge-based extraction as one possible implementation that shifts the focus from nodes to edges connecting pairs of nodes.

Building on the *positional tensors* $\mathbf{P} = \{\mathbf{P}_r, \mathbf{P}_\pi\}$ introduced in the node-based extraction, this edge-based method enables selective evaluation of promising moves while avoiding unnecessary computations. Specifically, we introduce a binary mask tensor $\mathbf{M} \in \{0, 1\}^{|\mathcal{V}| \times |\mathcal{V}|}$ to encode the outcome of neighborhood reduction. An entry $\mathbf{M}_{ij} = 1$ indicates that the edge (v_i, v_j) is valid under a given pruning criterion, and $\mathbf{M}_{ij} = 0$ otherwise. This mask restricts move evaluation to a reduced set of node pairs. Using the mask tensor \mathbf{M} together with the positional tensor \mathbf{P} , we retain only valid node pairs $\{(v_i, v_j) \mid \mathbf{M}_{ij} = 1\}$ and construct the corresponding *edge index tensors* $\mathbf{E} = \{\mathbf{E}_i, \mathbf{E}_j\}$. For each valid edge (v_i, v_j) , the tensors \mathbf{E}_i and \mathbf{E}_j store the positional information of

the source and target nodes, respectively, obtained by indexing \mathbf{P} as

$$\mathbf{E}_i = \mathbf{P}_i = \{\mathbf{P}_{r_i}, \mathbf{P}_{\pi_i}\}, \quad \mathbf{E}_j = \mathbf{P}_j = \{\mathbf{P}_{r_j}, \mathbf{P}_{\pi_j}\}, \quad \forall (i, j) \text{ such that } \mathbf{M}_{ij} = 1. \quad (16)$$

Based on these *edge index tensors*, the edge-based implementation of *3-Seq* operation extracts the *sequence attribute tensors* \mathbf{S}_h , \mathbf{S}_m , and \mathbf{S}_t following the same procedure as in the node-based extraction. Let E denote the number of selected edges (i.e., the number of nonzero entries in \mathbf{M}). The resulting intermediate and scoring tensors have size $O(E)$, yielding substantial reductions in memory consumption and computational cost compared to the node-based method.

In summary, we consider three extraction strategies for inter-route operators: route-based, node-based, and edge-based. As node-based extraction is more efficient than route-based (see the detailed analysis in Section 5.4), we define two standard TGA implementations: the node-implemented TGA (NTGA), which applies node-based extraction to inter-route operators with full neighborhood evaluation, and the edge-implemented TGA (ETGA), which uses edge-based extraction to enable neighborhood reduction. Both implementations use route-based extraction for intra-route operators.

5.3.2 Concatenation

After extracting the *sequence attribute tensors*, the extracted tensors are sliced along the first dimension to obtain the individual attribute tensors. The concatenation operation is then applied to these attribute tensors to construct the *neighbor attribute tensors*, which contain the attributes of the concatenated sequences and represent the neighboring solutions generated by the candidate moves.

$$\mathbf{D}(\mathbf{S}_1 \oplus \mathbf{S}_2) = \mathbf{D}(\mathbf{S}_1) + \mathbf{C}_{ij} + \mathbf{D}(\mathbf{S}_2) \quad (17a)$$

$$\mathbf{T}_D(\mathbf{S}_1 \oplus \mathbf{S}_2) = \mathbf{T}_D(\mathbf{S}_1) + \mathbf{T}_{ij} + \mathbf{\Delta}_w + \mathbf{T}_D(\mathbf{S}_2) \quad (17b)$$

$$i \in \mathbf{I}_e(\mathbf{S}_1), \quad j \in \mathbf{I}_s(\mathbf{S}_2) \quad (17c)$$

Let \mathbf{S}_1 and \mathbf{S}_2 denote the *sequence attribute tensors* of sequences σ_1 and σ_2 , respectively. Most attributes of the concatenated sequence can be computed directly using the tensorized formulas in Section 4.3, which only involve basic arithmetic operations and are therefore well-suited for GPU parallelization. However, the computation of travel distance and duration requires accounting for the additional costs of connecting the two sequences. Specifically, these costs can be derived from the travel distance tensor \mathbf{C} (corresponding to the travel distance matrix \mathcal{C}), the travel time tensor \mathbf{T} (corresponding to the travel time matrix \mathcal{T}), the last node index tensor of \mathbf{S}_1 ($\mathbf{I}_e(\mathbf{S}_1)$), and the first node index tensor of \mathbf{S}_2 ($\mathbf{I}_s(\mathbf{S}_2)$). The resulting concatenation formulas for

travel distance \mathbf{D} and duration \mathbf{T}_D are given in Equations (17a) and (17b), respectively, which correspond to Equations (2b) and (5e) in Section 4.3.

5.3.3 Differencing

To evaluate the effect of a candidate move, we compute the changes in key attributes between the current and modified routes. The attributes of the current routes are stored in the solution tensor \mathbf{T}_s , referred to as the *current attribute tensors*, while the attributes of the modified routes are obtained through the *Concatenation* step, referred to as *neighbor attribute tensors*. The differences are then computed element-wise to produce the *attribute delta tensors*, which include the changes in travel distance ($\Delta\mathbf{D}$), time window violations ($\Delta\mathbf{T}_V$), and load violations ($\Delta\mathbf{L}_V$). These attribute delta tensors form the input for the *Evaluation* step, enabling the tensorized computation of the *scoring tensor* \mathbf{F} for all candidate moves.

5.3.4 Evaluation

Building on the *attribute delta tensors* computed in the *Differencing* step, the *scoring tensor* \mathbf{F} is calculated using the defined evaluation function \mathcal{F} (Equation (18a)). Invalid entries are filtered via the boolean mask tensor \mathbf{B} by assigning a large penalty (Equation (18b)).

$$\mathbf{F} = \mathcal{F}(\Delta\mathbf{D}, \Delta\mathbf{T}_V, \Delta\mathbf{L}_V) \quad (18a)$$

$$\mathbf{F} \leftarrow \mathbf{F} + (\neg\mathbf{B}) \cdot \infty \quad (18b)$$

$$F_{\min} = \mathbf{F}_{\alpha^*} \quad \text{where} \quad \alpha^* = \arg \min_{\alpha} \mathbf{F}_{\alpha} \quad (18c)$$

Then, an *argmin* operation is applied to the *scoring tensor* \mathbf{F} to identify the best move with the minimal score value F_{\min} and its corresponding indices α^* (Equation (18c)). This operation is realized via a parallel *reduction* on the GPU. The indices α^* encode the information necessary to identify the best move, including the involved routes and the starting positions of the sequences to be relocated or swapped. Finally, this move information is transmitted to the CPU and used to update the solution S .

5.3.5 Tensor update

Once the best move is performed on the CPU, the solution tensor representation \mathbf{T}_s needs to be updated based on the resulting solution. Since the considered operators only impact one or two routes, only the affected parts of the tensor representation \mathbf{T}_s require updating, avoiding the need to reconstruct the entire tensor from scratch. Specifically, the update process consists of two main steps: (1) Resize the solution tensor \mathbf{T}_s if the maximum number of routes

J or the maximum route length K change. (2) Update the attribute values of the affected routes on the tensor representation \mathbf{T}_s on GPU. Additionally, the *positional tensors* $\mathbf{P} = \{\mathbf{P}_r, \mathbf{P}_\pi\}$ and the *edge index tensors* $\mathbf{E} = \{\mathbf{E}_i, \mathbf{E}_j\}$ also need to be updated accordingly if the node-based or edge-based extraction methods are used for inter-route operators.

5.4 Complexity analysis

We analyze the space and time complexity of the proposed tensor-based GPU acceleration (TGA) framework in terms of the number of tensor elements processed. We assume that up to p GPU threads can be scheduled in parallel. Let I be the number of maintained attributes, J the maximum number of routes, and K the maximum route length. Let L denote feasible length of the *sequence attribute tensors* in the route-based extraction. For inter-route operators, let $Q = M + N_C$ be the total number of valid nodes in the node-based extraction, and E the number of valid node pairs after neighborhood reduction in the edge-based extraction.

5.4.0.1 Tensor initialization and update The solution tensor $\mathbf{T}_s \in \mathbb{R}^{I \times J \times K \times K}$ requires $O(IJK^2)$ space and can be constructed on the GPU in $O(IJK^2/p)$ time. Since each accepted move modifies at most two routes, updating \mathbf{T}_s costs $O(IK^2)$ space and $O(IK^2/p)$ time.

When node-based or edge-based extraction is enabled for inter-route operators, the *positional tensors* $\mathbf{P} = \{\mathbf{P}_r, \mathbf{P}_\pi\}$ and the *edge index tensors* $\mathbf{E} = \{\mathbf{E}_i, \mathbf{E}_j\}$ must be updated. Updating the *positional tensors* \mathbf{P} has the complexity of $O(Q)$, whereas updating the *edge index tensors* \mathbf{E} requires generating valid node pairs based on the *positional tensors* \mathbf{P} and the mask tensor \mathbf{M} , and has a complexity of $O(Q^2)$, potentially becoming the bottleneck in the edge-based implementation.

Additionally, in practice, tensor initialization and updates involve data transfers between the CPU and GPU for building or updating the solution tensor \mathbf{T}_s . As a result, when tensor-based evaluation is relatively fast or the neighborhood size is small, data transfer overheads may dominate the total runtime despite the favorable complexity.

5.4.0.2 Tensor-based move evaluation Tensor-based move evaluation consists of four steps: *Extraction*, *Concatenation*, *Differencing*, and *Evaluation*. The *Extraction* step performs slicing, indexing, and reshaping operations on the solution tensor \mathbf{T}_s to obtain the *sequence attribute tensors*. The

Concatenation step constructs *neighbor attribute tensors* for each attribute independently, while the *Differencing* step computes *attribute delta tensors* for required attributes according to the evaluation function. Both of them involve element-wise arithmetic operations and broadcasting. These tensor operations involved in the first three steps can be highly parallelized on GPU. The *Evaluation* step computes the *scoring tensor* \mathbf{F} from the *attribute delta tensors* and identifies the best move via a *reduction* operation. This step has a time complexity of $O(n/p + \log p)$, where n denotes the number of elements in \mathbf{F} .

Based on the above analysis, Table 2 presents the dominant overall complexity and summarizes the per-step space and time complexity for route-based intra-route operators and for three extraction strategies of inter-route operators: route-based, node-based, and edge-based. The table shows that the

Table 2

Per-step space and time complexity of tensor-based move evaluation for intra-route operators (route-based), and inter-route operators (route-based, node-based, and edge-based).

Step	Intra-route (route-based)		Inter-route (route-based)		Inter-route (node-based)		Inter-route (edge-based)	
	Space	Time	Space	Time	Space	Time	Space	Time
Extraction	$O(IJL^2)$	$O\left(\frac{IJL^2}{p}\right)$	$O(IJL)$	$O\left(\frac{IJL}{p}\right)$	$O(IQ)$	$O\left(\frac{IQ}{p}\right)$	$O(IE)$	$O\left(\frac{IE}{p}\right)$
Concatenation	$O(IJL^2)$	$O\left(I\frac{JL^2}{p}\right)$	$O(IJ^2L^2)$	$O\left(I\frac{J^2L^2}{p}\right)$	$O(IQ^2)$	$O\left(I\frac{Q^2}{p}\right)$	$O(IE)$	$O\left(I\frac{E}{p}\right)$
Differencing	$O(JL^2)$	$O\left(\frac{JL^2}{p}\right)$	$O(J^2L^2)$	$O\left(\frac{J^2L^2}{p}\right)$	$O(Q^2)$	$O\left(\frac{Q^2}{p}\right)$	$O(E)$	$O\left(\frac{E}{p}\right)$
Evaluation	$O(JL^2)$	$O\left(\frac{JL^2}{p} + \log p\right)$	$O(J^2L^2)$	$O\left(\frac{J^2L^2}{p} + \log p\right)$	$O(Q^2)$	$O\left(\frac{Q^2}{p} + \log p\right)$	$O(E)$	$O\left(\frac{E}{p} + \log p\right)$
Overall	$O(IJL^2)$	$O\left(I\frac{JL^2}{p} + \log p\right)$	$O(IJ^2L^2)$	$O\left(I\frac{J^2L^2}{p} + \log p\right)$	$O(IQ^2)$	$O\left(I\frac{Q^2}{p} + \log p\right)$	$O(IE)$	$O\left(I\frac{E}{p} + \log p\right)$

overall computational cost is largely determined by the size of the *scoring tensor* \mathbf{F} . When \mathbf{F} is large, the *Evaluation* step dominates the computational cost; otherwise, the *Extraction* and *Concatenation* steps, particularly the latter, become the main contributors. For inter-route operators, the sizes satisfy $J^2L^2 > Q^2 > E$, due to the presence of the large number of invalid entries in the route-based implementation and the neighborhood reduction in the edge-based implementation. Consequently, the route-based implementation exhibits the highest space and time complexity. The node-based implementation significantly reduces complexity by restricting evaluation to valid nodes, while the edge-based implementation further improves computational efficiency by limiting evaluation to E valid node pairs, which is typically much smaller than Q^2 .

However, the edge-based implementation introduces additional overhead associated with constructing and maintaining the *edge index tensors* \mathbf{E} . Moreover, when neighborhood reduction is less effective, this approach may compromise solution quality. These trade-offs are examined in detail in the next section.

6 Computational results

This section presents computational experiments to evaluate the performance of the proposed tensor-based GPU acceleration (TGA) framework, focusing on two implementations: the node-implemented TGA (NTGA) and the edge-implemented TGA (ETGA), applied to common local search operators in vehicle routing problems.

It is important to note that the goal of this study is not to set new records for the benchmark instances. Instead, the goal is to explore the potential of the proposed TGA framework for solving vehicle routing problems and to provide a foundation for future research in this direction. Accordingly, the following sections focus on designing fair and consistent experiments to assess the effectiveness of the TGA framework, particularly in terms of computational efficiency, compared to traditional CPU-based implementations.

6.1 Algorithms for experimentation

This section describes the algorithms used to evaluate the proposed TGA framework. TGA is highly extensible and can be integrated into various local search-based algorithms. To demonstrate its effectiveness, we incorporated TGA into the MA-FIRD algorithm [31], which has shown its effectiveness in solving the VRPSPDTW. Since the CVRP and VRPTW are special cases of the VRPSPDTW, this integration allows the algorithm to address these variants as well, even though MA-FIRD was not originally designed for them. MA-FIRD employs a population-based evolutionary framework, feasible and infeasible search, the best-improvement local search strategy, and sequence concatenation-based move evaluation.

To evaluate TGA, we first adapted the original MA-FIRD algorithm of [31] as the baseline, denoted MA-N. Its TGA-based counterpart, referred to as MA-NTGA, integrates the proposed node-implemented TGA (NTGA) into MA-N. Both MA-N and MA-NTGA perform full neighborhood evaluation without applying neighborhood reduction of Section 5.3.1.4. To further assess the impact of neighborhood reduction in conjunction with TGA, we adopted two additional algorithm variants (MA-E and MA-ETGA) using the neighborhood reduction mechanism proposed in [33], with the granularity threshold θ controlling the number of nearest neighbors per node. Specifically, MA-E extends the CPU-based MA-N by incorporating neighborhood reduction into its local search operators, while MA-ETGA is its TGA-based counterpart, which integrates the edge-implemented TGA (ETGA) to support the same neighborhood reduction mechanism.

Table 3
 Characteristics of the four algorithm variants.

Algorithm	Move Evaluation	Neighborhood Reduction
MA-N	CPU-based	No
MA-E	CPU-based	Yes
MA-NTGA	TGA-based	No
MA-ETGA	TGA-based	Yes

As summarized in Table 3, these four algorithms (MA-N, MA-E, MA-NTGA, and MA-ETGA) share the same memetic algorithm framework, best-improvement local search strategy, and set of operators: *Relocate*, *Swap*, *2-opt** for the VRPTW and VRPSPDTW, plus *2-opt* for the CVRP. The only differences among them lie solely in their move evaluation implementations and the use of neighborhood reduction. A detailed description of these algorithms is provided in Section A2 of the supplementary material.

6.2 Benchmark instances

We assess the proposed TGA on three VRP variants: the capacitated VRP (CVRP), VRP with time windows (VRPTW), and the VRP with simultaneous pickup and delivery and time windows (VRPSPDTW), using widely recognized benchmark instances from the literature. Specifically, experiments were conducted on a representative subset of 210 benchmark instances across three VRP variants: 100 *X* benchmark instances [34] for CVRP, with 100 to 1000 customers; 20 *JD* benchmark instances [30] for VRPSPDTW, based on real-world JD Logistics data with 200, 400, 600, 800, and 1000 customers; and 90 selected *GH* instances for VRPTW, covering a wide range of sizes and characteristics. The *GH* benchmark [35] originally comprises 300 instances with 200 to 1000 customers, divided into three types: *C* (clustered), *R* (random), and *RC* (mixed), each including instances with both narrow and wide time windows and small and large vehicle capacities.

6.3 Experimental protocol

All four algorithm variants, MA-N, MA-E, MA-NTGA, and MA-ETGA, were implemented in C++, with the tensor-based GPU acceleration leveraging the PyTorch C++ API. The source code will be made publicly available upon publication of this paper. Experiments were performed on an Intel Xeon Gold 6248 2.50 GHz processor and an NVIDIA V100 GPU with 32 GB memory. As discussed in Section 3.1, the V100 is no longer state-of-the-art but remains a

mature and widely used GPU platform for algorithm evaluation. Importantly, since TGA is deterministic and hardware-independent, the GPU choice affects only runtime performance, and newer GPUs are expected to further improve efficiency without changing solution quality.

Our experimental design aims to provide a fair and consistent evaluation of TGA, with a particular focus on computational gains over traditional CPU-based implementations. To ensure controlled comparisons, the algorithmic parameters were adopted from MA-FIRD [31] and kept consistent across all variants, avoiding biases due to differing configurations. Key parameters, including the population size μ and the granularity threshold θ (introduced in MA-E and MA-ETGA), were tuned using the automatic parameter configuration tool Irace [36] on a selected subset of instances from each benchmark. Table 4 reports the candidate ranges and selected values for each benchmark set.

Table 4
Parameter tuning results.

Parameter	Description	Candidate values	X	GH	JD
μ	Population size	{10, 20, 30, 40, 50}	40	10	10
θ	Granularity threshold	{20, 50, 80, 100, 120}	20	100	80

To ensure fair comparisons with state-of-the-art methods, we adopt the same termination criteria as in the corresponding studies for each benchmark set. For the X (CVRP) instances, the time limit is proportional to the number of customers, set to $N_C \times 240/100$ seconds [37,14]. For the GH (VRPTW) instances, the limits are 1800, 3600, and 7200 seconds for instances with ≤ 200 , ≤ 800 , and > 800 customers, respectively [38]. For the JD (VRPSPDTW) instances, following [31], termination occurs when any of the following criteria is met: a maximum of 5000 generations, 500 consecutive generations without improvement, or a time limit of 7200 seconds. Each instance was solved 10 times by each algorithm variant.

6.4 Computational results and comparisons

Figure 10 compares the average computation time and average gap of MA-E, MA-NTGA, and MA-ETGA relative to the baseline MA-N across 210 instances of three benchmark sets: X (CVRP), GH (VRPTW), and JD (VRPSPDTW). The average gap is defined as the relative difference in objective value with respect to MA-N, with detailed numerical results reported in Tables A3-A7 in the supplementary material. Overall, all three variants outperform MA-N, while the TGA-based algorithms further improve upon both

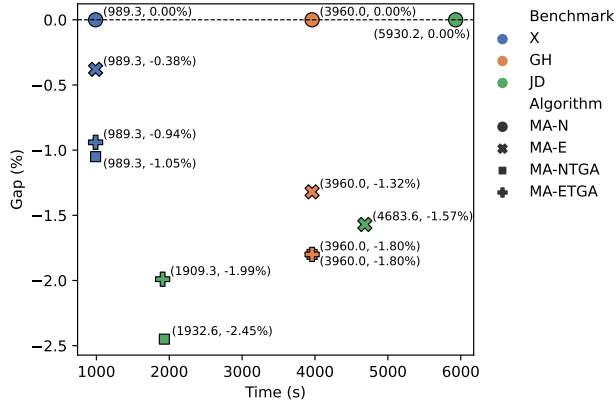


Fig. 10. Comparative performance of MA-N, MA-E, MA-NTGA, and MA-ETGA on three benchmark sets. The x-axis shows average computation time (s), and the y-axis shows average gap (%) relative to the baseline MA-N.

MA-N and MA-E across all benchmarks. For the X and GH instances, where termination is solely time-based, performance differences are clearly reflected in the gap values. On X , MA-NTGA and MA-ETGA achieve average gaps of -1.05% and -0.94%, respectively, compared to -0.38% for MA-E. On GH , both MA-NTGA and MA-ETGA attain average gaps of -1.80%, outperforming MA-E’s -1.32%. For the JD instances, which additionally use generation-based and stagnation-based stopping criteria, MA-NTGA and MA-ETGA achieve larger improvements (-2.45% and -1.99%) than MA-E (-1.57%), while requiring shorter average computation times. These results demonstrate both the computational efficiency and enhanced search capability of the TGA-based implementations.

MA-NTGA and MA-ETGA exhibit comparable performance, with MA-NTGA showing a slight advantage. This suggests that although the edge-implemented TGA (ETGA) effectively accelerates move evaluation by reducing the neighborhood size, it does not automatically translate into superior solution quality. The effectiveness of neighborhood reduction strongly depends on its design, inappropriate pruning may eliminate promising high-quality moves. Moreover, the edge-based implementation introduces extra overhead, affecting overall efficiency, which is analyzed in detail in the following section.

6.5 Analysis of overall speedup ratio

To provide an intuitive assessment of the performance gains achieved by TGA-based algorithms over their traditional CPU-based counterparts, we conducted additional experiments to measure speedup ratios for move evaluation across benchmark instances. Let t_{CPU} denote the total runtime spent on move evaluations of the CPU-based algorithms (MA-N and MA-E) after 100 iterations, and

t_{TGA} the corresponding runtime for the TGA implementations (MA-NTGA and MA-ETGA) under the same iteration budget. The speedup ratio is defined as $\gamma_s = \frac{t_{\text{CPU}}}{t_{\text{TGA}}}$. Each instance was executed 10 times, with paired algorithm variants (MA-N vs. MA-NTGA and MA-E vs. MA-ETGA) following identical search trajectories in each run to ensure fair and consistent comparisons. Figure 11 reports the resulting speedup ratios across all tested instances, highlighting the relationship between instance size and speedup ratio for different benchmark instances.

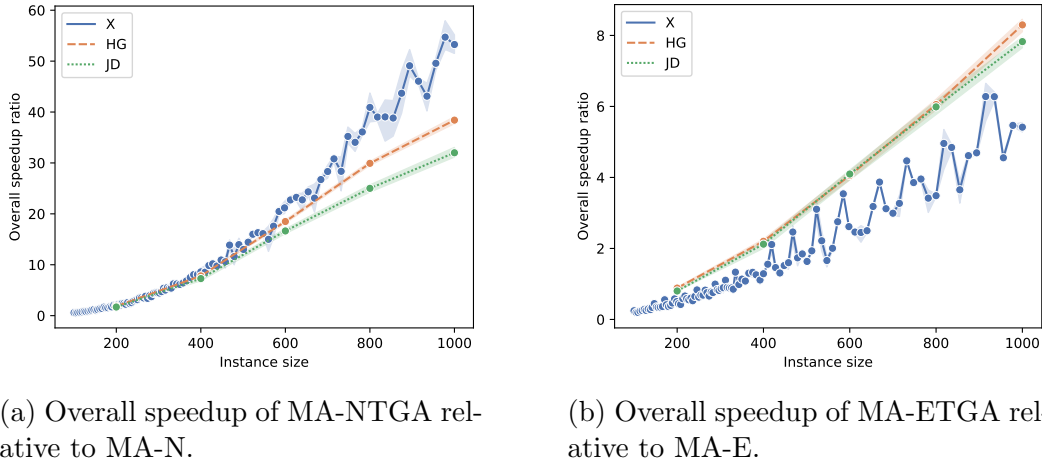


Fig. 11. Relationship between instance size and speedup ratio across benchmark instances. The x-axis denotes the instance size, while the y-axis reports the speedup of TGA-based algorithms over their CPU-based counterparts.

The experimental results reveal a clear positive correlation between instance size and speedup ratio across all benchmarks. For the *GH* (VRPTW) and *JD* (VRPSPDTW) instances, both TGA variants exhibit monotonic speedup growth as instance size increases. In particular, MA-NTGA achieves substantial acceleration, with speedup ratios rising from approximately 2 to over 30 when scaling from 200 to 1000 nodes, consistent with theoretical expectations and demonstrating the effectiveness of TGA on large-scale instances. MA-ETGA follows the same trend but with smaller speedup ratios (from about 1 to over 8), as MA-E already reduces move evaluation via neighborhood reduction, leaving less exploitable parallelism for TGA.

A similar trend is observed for the *X* (CVRP) benchmark, where MA-NTGA achieves even higher acceleration on large instances due to the less constrained nature of CVRP, with speedups exceeding $50\times$ on approximately 1000-node instances. In contrast, no noticeable acceleration is observed for small (around 100-node) instances, where GPU overhead outweighs the performance gains, underscoring that TGA is most beneficial for large and computationally intensive problems. For MA-ETGA on *X* instances, the speedup ratios are substantially lower, as MA-E already eliminates a large portion of move evalua-

tions under the granularity threshold $\theta = 20$, leaving limited scope for further acceleration by TGA. Additionally, some variability in speedup is observed among X instances, which can be attributed to instance-specific characteristics, particularly the number of vehicles. As discussed in Section 5.4, instances requiring more vehicles generate larger scoring tensors, which increases the computational cost to indentify the best move.

6.6 Acceleration of move evaluation across operators

We further analyze TGA performance at the operator level by examining speedup gains across benchmark instances of varying sizes. Figure 12 shows the speedup ratios for different local search operators, which are calculated as the average runtime of move evaluation for the CPU-based implementation divided by that of the corresponding TGA-based implementation.

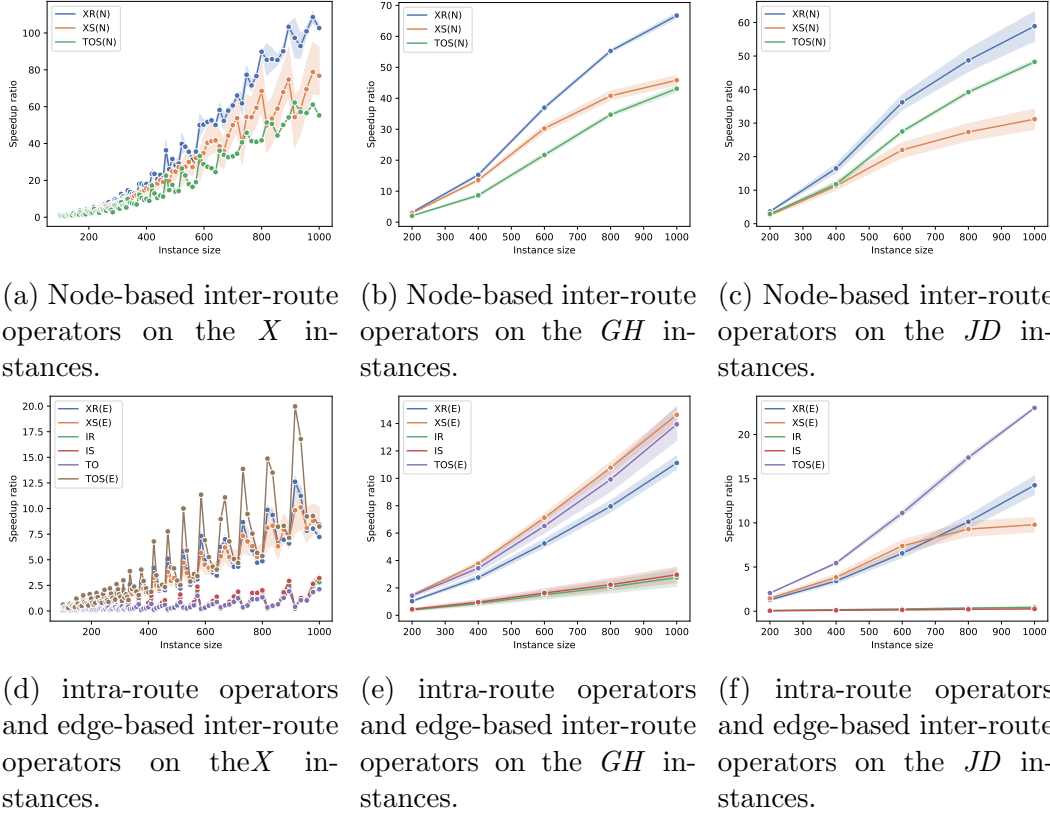
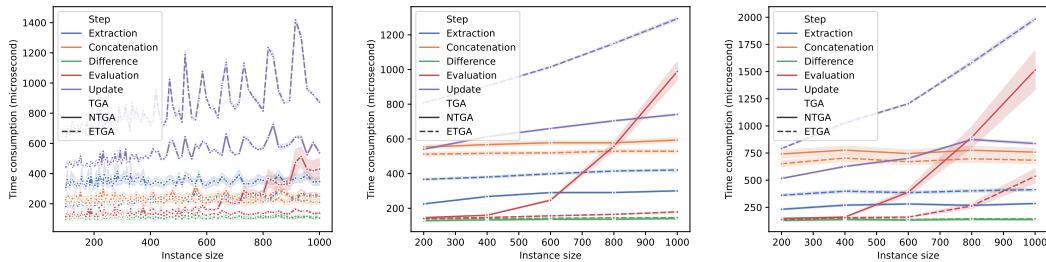


Fig. 12. Speedup ratios of local search operators across benchmark instances, including inter-route operators (*Inter-Relocate*, *Inter-Swap*, 2-opt^*) with node-based (XR(N), XS(N), TOS(N)) and edge-based implementations (XR(E), XS(E), TOS(E)), as well as route-based intra-route operators (*Intra-Relocate* (IR), *Intra-Swap* (IS), 2-opt (TO)). The x-axis denotes instance size and the y-axis the corresponding speedup ratio.

Overall, the speedup ratio increases with instance size. TGA achieves particularly significant acceleration for inter-route operators (*Inter-Relocate*, *Inter-Swap*, *2-opt**), which involve complex cross-route interactions and benefit strongly from GPU parallelization. Node-based implementations reach speedups from 2 up to over 60 for the *GH* and *JD* instances, and exceed 100 for around 1000-node *X* instances. Edge-based implementations also achieve substantial speedups, though slightly lower, as neighborhood reduction strategy already reduces many move evaluations, leaving less room for additional acceleration. In contrast, intra-route operators (*Intra-Relocate*, *Intra-Swap*, *2-opt*) show more modest gains, with speedups up to around 2 for large 1000-node instances. This contrast highlights the particular advantage of the TGA framework for inter-route operators, which require more complex cross-route computations.

6.7 Time analysis of key steps in TGA

To complement the theoretical complexity analysis in Section 5.4, we examine the practical runtime of TGA’s key steps (*Extraction*, *Concatenation*, *Differencing*, *Evaluation*, and *Update*) defined in Section 5.3. Figure 13 reports the time consumption of each step across varying instance sizes for both NTGA and ETGA.



(a) Time consumption of TGA’s key steps for different instance sizes on *X* instances. (b) Time consumption of TGA’s key steps for different instance sizes on *GH* instances. (c) Time consumption of TGA’s key steps for different instance sizes on *JD* instances.

Fig. 13. Time analysis of TGA’s key steps for varying instance sizes. The x-axis indicates instance size, and the y-axis represents computation time for each step.

Across all three benchmarks, tensor-based move evaluation steps *Extraction*, *Concatenation*, and *Differencing* show relatively stable runtimes, reflecting near-constant complexity. In contrast, *Evaluation* shows the largest variability, as its cost scales with the size of the *scoring tensor*, which depends on instance characteristics such as the number of customers and vehicles. Therefore, for inter-route operators with large neighborhoods and complex cross-route interactions, *Evaluation* dominates the overall runtime. For intra-route

operators, the smaller neighborhoods substantially reduce the *Evaluation* cost, making *Extraction* and *Concatenation* more prominent. Additionally, a clear distinction is observed between NTGA and ETGA in terms of *Evaluation* step. By restricting the effective neighborhood through edge-based implementation, ETGA significantly reduces the *Evaluation* time, particularly on large instances. Finally, the *Update* step emerges as a non-negligible and increasing cost, especially for large instances and in the ETGA. *Update* step involves GPU-CPU synchronization, data transfer, and the update of the solution tensor. In ETGA, this cost is further amplified by the maintenance of *edge index tensors*. Moreover, as ETGA substantially shortens the *Evaluation* step, these fixed overheads account for a larger fraction of the total runtime, making *Update* both absolutely and relatively more expensive.

Overall, this analysis identifies the primary performance bottlenecks of TGA. In NTGA, *Evaluation* dominates due to full neighborhood exploration, whereas in ETGA, the substantial reduction in *Evaluation* time makes *Update* the dominant cost for large-scale instances. These observations suggest potential avenues for performance improvement in future work.

6.8 Comparative analysis with algorithms in the literature

Although this study does not aim to achieve new best-known solutions (BKS), we provide a comparative analysis of the proposed TGA-based algorithms (MA-NTGA and MA-ETGA) against leading methods from the literature. For the CVRP and VRPTW, BKS values are taken from the CVRPLIB repository (<http://vrp.galgos.inf.puc-rio.br/>) as of December 25, 2025. CVRP comparisons include HGS-2012 [37] and HGS-CVRP [14]. For the VRPTW, with the objective of minimizing the total travel distance, comparisons include the DIMACS competition reference results and the champion algorithm HGS-DIMACS [38]. For VRPSPDTW, we report results from the state-of-the-art MA-FIRD method [31]. MA-NTGA and MA-ETGA results correspond to the best solutions in Section 6.4, with all algorithms evaluated under the same termination criteria as reported in their respective references. Although our TGA-based algorithms leverage GPU acceleration while reference algorithms are CPU-based, the CPU specifications provided in the supplementary material indicate that processor performance is broadly comparable.

Figure 14 summarizes the results, with detailed numerical results reported in Tables A8-A12 in the supplementary material. On the *JD* instances, MA-NTGA and MA-ETGA achieve competitive performance, with mean gaps of -0.66% and -0.27% relative to BKS in shorter computation times. For the *X* (CVRP) and *GH* (VRPTW) instances, the TGA-based algorithms exhibit larger gaps compared to state-of-the-art methods. Specifically, MA-NTGA

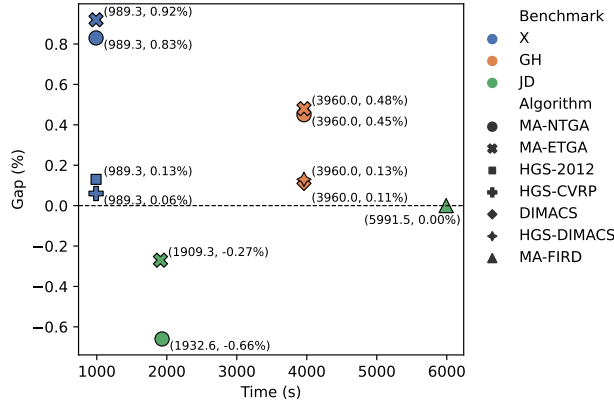


Fig. 14. Comparative performance of TGA-based algorithms and state-of-the-art methods on benchmark instances. The x-axis shows average computation time (s), and the y-axis shows gap (%) relative to the BKS.

attains mean gaps of 0.83% on X and 0.45% on GH , while MA-ETGA achieves 0.92% and 0.48% on the same benchmarks, respectively. These results indicate that TGA-based algorithms do not achieve top-tier performance on these two benchmarks, which is expected and can be reasonably explained by several factors.

First, the TGA-based algorithms are built on MA-FIRD, originally designed for the more complex VRPSPDTW rather than for the CVRP or VRPTW. This is particularly impactful for the relatively simpler CVRP, where such sophisticated algorithmic components are not strictly necessary, thereby limiting the competitiveness of TGA-based algorithms on these instances. Second, our algorithms employ a limited set of basic local search operators within the TGA framework, whereas state-of-the-art algorithms typically integrate richer and advanced operators, such as SWAP* [14] and RELOCATE* [38], which significantly enhance solution quality and search capability. Third, MA-NTGA relies on a best-improvement strategy without neighborhood reduction. Although MA-ETGA introduces neighborhood reduction through an edge-based implementation, it remains more constrained than the sophisticated pruning techniques adopted by state-of-the-art algorithms, which are critical to accelerate the search process and improve search efficiency. Taken together, these factors explain the performance gap observed on the X and GH instances.

In summary, while TGA-based algorithms do not yet match leading CPU-based methods, they demonstrate the potential of the TGA framework and GPU-based approaches for vehicle routing problems, providing a promising foundation for future improvements.

7 Discussion

The TGA framework demonstrates strong extensibility and adaptability. Its attribute-based solution tensor representation allows it to handle a wide range of VRP variants by maintaining problem-specific attribute matrices. Even for more complex VRP variants involving additional decision-making beyond route optimization, such as the multi-depot VRP, the periodic VRP, and the location routing problem, TGA can efficiently optimize the routing component. Its low-coupling architecture fully offloads intensive computations to the GPU, allowing seamless integration into existing local search-based algorithms.

Building on the tensorized implementation of basic local search operators, TGA also supports more advanced operators. For example, *Relocate* and *Swap* can incorporate reversed subsequences by exchanging the first and last node index tensors, as in *2-opt*. Multi-route sequence exchanges can be accommodated by adding tensor dimensions, and filtering strategies, such as tabu-like mechanisms, can be implemented via mask tensors to exclude irrelevant moves.

TGA also exhibits several limitations. Speedups for intra-route operators are less pronounced than for inter-route operators, indicating room for improvement. In node-implemented TGA, the efficiency of the *Evaluation* step is sensitive to the size of the *scoring tensor*. Edge-implemented TGA mitigates this by restricting the neighborhood but introduces additional overhead in the *Update* step due to maintaining *edge index tensors*. These trade-offs suggest that the current solution tensor design does not yet fully support advanced neighborhood reduction techniques commonly used in CPU-based local search. Exploring alternative representations that better accommodate such mechanisms is a promising direction for future work.

Overall, TGA provides a promising direction for leveraging GPU parallelism for solving challenging routing problems. However, comparisons with state-of-the-art algorithms show that it remains early-stage relative to mature CPU-based implementations, with substantial room for improvement in both solution quality and search efficiency. Rather than directly replicating CPU-oriented search strategies which are inherently designed and optimized for CPU architectures, future research should develop search strategies tailored to TGA’s parallel execution model. For example, moves are currently evaluated in parallel on the GPU, but acceptance remains sequential, with only one move applied per iteration. In contrast, methods like *Dynasearch* [39] use dynamic programming to identify optimal combinations of multiple independent moves within the neighborhood. Adapting similar ideas could better exploit TGA’s massive parallelism to apply multiple moves simultaneously, enhancing both efficiency and solution quality.

Furthermore, the principles of TGA extend beyond local search and can benefit a wide range of optimization methods. Population-based metaheuristics can leverage parallel evaluation and manipulation of multiple solutions on GPUs, while exact methods can exploit tensor representations of partial solutions or subproblems to evaluate feasibility, bounds, and branching decisions in parallel. This approach accelerates traditionally sequential processes such as branch-and-bound or dynamic programming, offering high computational efficiency while maintaining optimality. More broadly, TGA’s philosophy can be applied to other combinatorial optimization problems, improving both algorithmic efficiency and performance.

8 Conclusion

This work proposes a Tensor-based GPU Acceleration framework, along with two implementations, node-implemented TGA and edge-implemented TGA, for accelerating common local search operators in vehicle routing problems. By leveraging fine-grained GPU parallelism, the proposed framework significantly accelerates neighborhood exploration, which is one of the main computational bottlenecks in local search-based algorithms.

Extensive experiments on three routing problems, CVRP, VRPTW, and VRP-SPDTW, confirm the effectiveness and efficiency of our proposed framework, achieving remarkable performance improvements and computational efficiency gains on benchmark instances compared to traditional CPU-based implementations. In-depth analyses of operator-level acceleration and the key steps within the framework valuable insights and reveal critical bottlenecks for future improvement.

Due to its low-coupling architecture and strong extensibility, the TGA framework can be seamlessly integrated into various local search-based routing algorithms, offering a powerful and efficient tool for solving a wide range of vehicle routing problem variants. Beyond vehicle routing, the generality of its attribute-based representation and tensorized evaluation pipeline suggests strong potential for extending the framework to other combinatorial optimization problems and methods. Future work will focus on refining the framework, enhancing GPU utilization, and exploring broader applications within and beyond routing problems.

Acknowledgments

This work was granted access to the HPC resources of IDRIS under the allocation 2025-AD010617072 made by GENCI. We also acknowledge the HPC resources provided by the Centre de Calcul Intensif des Pays de la Loire (CCIPL), France.

References

- [1] G. B. Dantzig, J. H. Ramser, The truck dispatching problem, *Management Science* 6 (1) (1959) 80–91.
- [2] G. Clarke, J. W. Wright, Scheduling of vehicles from a central depot to a number of delivery points, *Operations Research* 12 (4) (1964) 568–581.
- [3] J. K. Lenstra, A. Rinnooy Kan, Complexity of scheduling under precedence constraints, *Operations Research* 26 (1) (1978) 22–35.
- [4] G. Laporte, The vehicle routing problem: An overview of exact and approximate algorithms, *European Journal of Operational Research* 59 (3) (1992) 345–358.
- [5] J. Andelmin, E. Bartolini, An exact algorithm for the green vehicle routing problem, *Transportation Science* 51 (4) (2017) 1288–1303.
- [6] R. Praxedes, T. Bulhões, A. Subramanian, E. Uchoa, A unified exact approach for a broad class of vehicle routing problems with simultaneous pickup and delivery, *Computers & Operations Research* 162 (2024) 106467.
- [7] W.-C. Chiang, R. A. Russell, Simulated annealing metaheuristics for the vehicle routing problem with time windows, *Annals of Operations Research* 63 (1996) 3–27.
- [8] E. Rodríguez-Esparza, A. D. Masegosa, D. Oliva, E. Onieva, A new hyper-heuristic based on adaptive simulated annealing and reinforcement learning for the capacitated electric vehicle routing problem, *Expert Systems with Applications* 252 (2024) 124197.
- [9] P. Toth, D. Vigo, The granular tabu search and its application to the vehicle-routing problem, *Informatics Journal on Computing* 15 (4) (2003) 333–346.
- [10] M. Gmira, M. Gendreau, A. Lodi, J.-Y. Potvin, Tabu search for the time-dependent vehicle routing problem with time windows on a road network, *European Journal of Operational Research* 288 (1) (2021) 129–140.
- [11] B. M. Baker, M. Ayechev, A genetic algorithm for the vehicle routing problem, *Computers & Operations Research* 30 (5) (2003) 787–800.

- [12] A. S. Tasan, M. Gen, A genetic algorithm based approach to vehicle routing problem with simultaneous pick-up and deliveries, *Computers & Industrial Engineering* 62 (3) (2012) 755–761.
- [13] D. Cattaruzza, N. Absi, D. Feillet, T. Vidal, A memetic algorithm for the multi trip vehicle routing problem, *European Journal of Operational Research* 236 (3) (2014) 833–848.
- [14] T. Vidal, Hybrid genetic search for the cvrp: Open-source implementation and swap* neighborhood, *Computers & Operations Research* 140 (2022) 105643.
- [15] G. Laporte, Fifty years of vehicle routing, *Transportation Science* 43 (4) (2009) 408–416.
- [16] T. Vidal, T. G. Crainic, M. Gendreau, C. Prins, Heuristics for multi-attribute vehicle routing problems: A survey and synthesis, *European Journal of Operational Research* 231 (1) (2013) 1–21.
- [17] K. Braekers, K. Ramaekers, I. Van Nieuwenhuysse, The vehicle routing problem: State of the art classification and review, *Computers & Industrial Engineering* 99 (2016) 300–313.
- [18] S.-Y. Tan, W.-C. Yeh, The vehicle routing problem: State-of-the-art classification and review, *Applied Sciences* 11 (21) (2021) 10295.
- [19] M. H. Rashid, I. McAndrew, An efficient gpu framework for parallelizing combinatorial optimization heuristics, in: *2020 International Conference on Advances in Computing and Communication Engineering*, IEEE, 2020, pp. 1–7.
- [20] J. R. Cheng, M. Gen, Accelerating genetic algorithms with gpu computing: A selective overview, *Computers & Industrial Engineering* 128 (2019) 514–525.
- [21] O. Goudet, J.-K. Hao, A massively parallel evolutionary algorithm for the partial latin square extension problem, *Computers & Operations Research* 158 (2023) 106284.
- [22] O. Goudet, A. Goëffon, J.-K. Hao, A large population island framework for the unconstrained binary quadratic problem, *Computers & Operations Research* 168 (2024) 106684.
- [23] B. Nogueira, W. Rosendo, E. Tavares, E. Andrade, Gpu tabu search: a study on using gpu to solve massive instances of the maximum diversity problem, *Journal of Parallel and Distributed Computing* (2024) 105012.
- [24] M. F. Abdelatti, M. S. Sodhi, An improved gpu-accelerated heuristic technique applied to the capacitated vehicle routing problem, in: *Proceedings of the 2020 Genetic and Evolutionary Computation Conference*, 2020, pp. 663–671.
- [25] Z. Zhang, Y. Sun, H. Xie, Y. Teng, J. Wang, Gmma: Gpu-based multiobjective memetic algorithms for vehicle routing problem with route balancing, *Applied Intelligence* 49 (2019) 63–78.

- [26] C. Schulz, Efficient local search on the gpu—investigations on the vehicle routing problem, *Journal of Parallel and Distributed Computing* 73 (1) (2013) 14–31.
- [27] P. Yelmewad, B. Talawar, Gpu-based parallel heuristics for capacited vehicle routing problem, in: *2020 IEEE International Conference on Electronics, Computing and Communication Technologies*, IEEE, 2020, pp. 1–6.
- [28] I. Coelho, P. Munhoz, L. S. Ochi, M. Souza, C. Bentes, R. Farias, An integrated cpu–gpu heuristic inspired on variable neighbourhood search for the single vehicle routing problem with deliveries and selective pickups, *International Journal of Production Research* 54 (4) (2016) 945–962.
- [29] T. Vidal, T. G. Crainic, M. Gendreau, C. Prins, A unified solution framework for multi-attribute vehicle routing problems, *European Journal of Operational Research* 234 (3) (2014) 658–673.
- [30] S. Liu, K. Tang, X. Yao, Memetic search for vehicle routing with simultaneous pickup-delivery and time windows, *Swarm and Evolutionary Computation* 66 (2021) 100927.
- [31] Z. Lei, J.-K. Hao, A memetic algorithm for vehicle routing with simultaneous pickup and delivery and time windows, *IEEE Transactions on Evolutionary Computation* (Early Access), DOI: 10.1109/TEVC.2024.3456585 (2024) 1–1.
- [32] Y. Nagata, O. Bräysy, W. Dullaert, A penalty-based edge assembly memetic algorithm for the vehicle routing problem with time windows, *Computers & Operations Research* 37 (4) (2010) 724–737.
- [33] T. Vidal, T. G. Crainic, M. Gendreau, C. Prins, A hybrid genetic algorithm with adaptive diversity management for a large class of vehicle routing problems with time-windows, *Computers & Operations Research* 40 (1) (2013) 475–489.
- [34] E. Uchoa, D. Pecin, A. Pessoa, M. Poggi, T. Vidal, A. Subramanian, New benchmark instances for the capacitated vehicle routing problem, *European Journal of Operational Research* 257 (3) (2017) 845–858.
- [35] H. Gehring, J. Homberger, A parallel hybrid evolutionary metaheuristic for the vehicle routing problem with time windows, in: *Proceedings of EUROGEN99*, Vol. 2, Springer, 1999, pp. 57–64.
- [36] M. López-Ibáñez, J. Dubois-Lacoste, L. P. Cáceres, M. Birattari, T. Stützle, The irace package: Iterated racing for automatic algorithm configuration, *Operations Research Perspectives* 3 (2016) 43–58.
- [37] T. Vidal, T. G. Crainic, M. Gendreau, N. Lahrichi, W. Rei, A hybrid genetic algorithm for multidepot and periodic vehicle routing problems, *Operations Research* 60 (3) (2012) 611–624.
- [38] W. Kool, J. O. Juninck, E. Roos, K. Cornelissen, P. Agterberg, J. van Hoorn, T. Visser, Hybrid genetic search for the vehicle routing problem with time windows: A high-performance implementation, in: *12th*

DIMACS Implementation Challenge Workshop, DIMACS, Rutgers University
Piscataway, NJ, 2022.

- [39] R. K. Congram, C. N. Potts, S. L. van de Velde, An iterated dynasearch algorithm for the single-machine total weighted tardiness scheduling problem, *INFORMS Journal on Computing* 14 (1) (2002) 52–67.

Supplementary materials of paper “Speeding up Local Optimization in Vehicle Routing with Tensor-based GPU Acceleration”

This document provides supplementary materials for the paper “Speeding up Local Optimization in Vehicle Routing with Tensor-based GPU Acceleration”. It contains the notation table, the algorithmic framework of the tested algorithms, and detailed computational results for both the proposed algorithm variants and the state-of-the-art comparisons.

A1 Notation

Table A2 summarizes the key notation used throughout the paper. Note that tensors are uniformly denoted by bold capital letters (e.g., \mathbf{T}_s).

A2 Algorithmic framework of the tested algorithms

This section presents an overview of the algorithms used in the comparative study to evaluate the performance of the proposed tensor-based GPU acceleration (TGA) framework.

The TGA framework is highly extensible and can be integrated into various local search based algorithms. To demonstrate its effectiveness, we incorporate TGA into the MA-FIRD algorithm [31], which has shown its effectiveness in solving the VRPSPDTW. Since both the CVRP and the VRPTW can be considered special cases of the VRPSPDTW, this integration allows the algorithm to address these variants as well.

MA-FIRD of [31] is a memetic algorithm that combines a feasible and infeasible route descent search (FIRD) and an adaptive route-inheritance crossover (ARIX). The FIRD procedure is a local search procedure using the best-improvement strategy and the sequence concatenation-based move evaluation method. The ARIX crossover generates offspring solutions by inheriting routes from multiple parent solutions and incorporates a learning mechanism to adaptively adjust the number of parents and the heuristics used to complete the partial offspring under construction.

To evaluate the performance of TGA, we modified the initial MA-FIRD algorithm of [31] and incorporated TGA. The resulting general MA framework is illustrated in Algorithm 1. For a given problem instance \mathcal{I} , the algorithm begins by generating an initial population \mathcal{P} consisting of μ candidate solutions

(line 4), with the best solution S^* being recorded (line 5). The algorithm then iteratively updates the population by creating new candidate solutions (lines 6-18). In each generation, the adaptive route-inheritance crossover ARIX generates a new solution S (line 7), which is then improved using feasible and infeasible search based on the given local search operators in \mathcal{O} (line 8). Note that the route descent strategy is omitted in this setting to simplify the search process and ensure compatibility with problem variants that do not consider the number of vehicles as an objective. The improved solution S is used to update the population according to the population management strategy (line 9). If an improved best solution is found, S^* is updated, and the stagnation counter is reset to zero (lines 11-13). Otherwise, the stagnation generation counter φ_{st} increments (lines 14-15). The algorithm terminates and returns the best solution S^* (line 19) when the given termination condition is reached (line 6).

Algorithm 1 General MA framework

```

1: Input: Instance  $\mathcal{I}$ , population size  $\mu$ , set of operators  $\mathcal{O} = \{O_1, O_2, \dots, O_n\}$ .
2: Output: The best solution  $S^*$ .
3:  $\varphi \leftarrow 0, \varphi_{st} \leftarrow 0$  /* Current generation and stagnation generation counter */
4:  $\mathcal{P} \leftarrow Initialization(\mathcal{I}, \mu)$ 
5:  $S^* \leftarrow BestSolution(\mathcal{P})$  /* Record current best solution */
6: while The given termination condition is not met do
7:    $S \leftarrow ARIX(\mathcal{P})$ 
8:    $S \leftarrow FeasibleInfeasibleSearch(S, \mathcal{O})$ 
9:    $\mathcal{P} \leftarrow UpdatePopulation(S, \mathcal{P})$ 
10:   $S_{best} \leftarrow BestSolution(\mathcal{P})$  /* The best solution in this generation */
11:  if  $f(S_{best}) < f(S^*)$  then
12:     $S^* \leftarrow S_{best}$  /* Update the best solution */
13:     $\varphi_{st} \leftarrow 0$ 
14:  else
15:     $\varphi_{st} \leftarrow \varphi_{st} + 1$  /* Stagnation counter is incremented */
16:  end if
17:   $\varphi = \varphi + 1$ 
18: end while
19: return  $S^*$ 

```

Within the MA framework, the feasible and infeasible search constitutes the core local search component responsible for search intensification and distinguishes the four algorithmic variants considered in our comparative study. Algorithm 2 presents the general procedure of the feasible and infeasible search for the TGA-based algorithms (MA-NTGA and MA-ETGA), in which the proposed tensor-based GPU acceleration is employed for move evaluation (line 6). In contrast, their CPU-based counterparts (MA-N and MA-E) exclude lines

Algorithm 2 Feasible and infeasible search

```
1: Input: Input solution  $S$ , set of operators  $\mathcal{O} = \{O_1, O_2, \dots, O_n\}$ .
2: Output: Improved solution  $S$ .
3: Initialize tensor  $\mathbf{T}_s$  on GPU based on the solution  $S$ .
4: while The given termination criterion is not met do
5:   Select an operator  $O_i \in \mathcal{O}$ .
6:    $\zeta \leftarrow Evaluate(\mathbf{T}_s, S, O_i)$  /*Evaluate the neighborhood of the operator
    $O_i$  and obtain the best move  $\zeta^*$ /.
7:   if The move  $\zeta$  is accepted based on the defined evaluation then
8:     Update current solution  $S$  based on the move  $\zeta$ .
9:     Update tensor  $\mathbf{T}_s$  based on current solution  $S$ .
10:  end if
11: end while
12: return  $S$ 
```

3 and 9 of Algorithm 2 and rely on traditional CPU implementations of the local search operators for move evaluation (line 6). Both the TGA-based and CPU-based algorithms adopt the same best-improvement local search strategy. MA-N and MA-NTGA evaluate the full neighborhood without reduction, whereas MA-E and MA-ETGA apply neighborhood reduction.

A3 Detailed computational results

Tables A3-A7 present detailed computational results based on 10 runs for four algorithm variants, MA-N, MA-E, MA-NTGA, and MA-ETGA, which are evaluated on three benchmark sets: 100 X (CVRP) instances [34], 90 selected GH (VRPTW) instances [35], and 20 JD (VRPSPDTW) instances [30].

MA-N and MA-E are CPU-based algorithms employing traditional local search evaluation methods, whereas MA-NTGA and MA-ETGA integrate the proposed tensor-based GPU acceleration (TGA). MA-N serves as the baseline algorithm for performance comparison.

Each table reports the instance name (*Instance*), the number of customers (N_C), the average number of vehicles (M), the best objective value (f^*), and the average objective value (f) over 10 independent runs for each algorithm variant. The column “Gap(%)” indicates the percentage improvement in average objective value relative to MA-N, where a negative value corresponds to better performance.

For the X (CVRP) and GH (VRPTW) instances, the unified termination conditions with time limits from the literature [37,14,38] are adopted, and the

corresponding limits are reported in column t (in seconds). For the JD (VRP-SPDTW) instances, compound termination conditions are applied following [31], and the actual average computation times are reported in column t .

A4 Detailed computational results for the state-of-the-art comparisons

This section provides detailed comparative results between the proposed TGA-based algorithms (MA-NTGA and MA-ETGA) and state-of-the-art methods on three benchmark sets: X (CVRP), GH (VRPTW), and JD (VRPSPDTW). Although our TGA-based algorithms leverage GPU acceleration while reference algorithms are CPU-based, Table A1 reports PassMark CPU benchmark scores (<https://www.passmark.com/>) for both our experimental CPU and those used in the reference studies. The reported differences show that our CPU performance is within $\pm 10\%$ of the references, indicating broadly comparable CPU performance.

Table A1

Processor specifications and corresponding CPU benchmark scores.

Algorithm	Processor	Base frequency	CPU mark	Difference (%)
HGS-2012	Intel Xeon Gold 6148	2.40 GHz	2072	-8.2%
HGS-CVRP	Intel Xeon Gold 6148	2.40 GHz	2072	-8.2%
HGS-DIMACS	Intel Core i7-6850K	3.60 GHz	2388	+5.8%
MA-FIRD	Intel Xeon E5-2690 v4	2.60 GHz	2069	-8.3%
Ours	Intel Xeon Gold 6248	2.50 GHz	2257	0%

Tables A8-A12 show detailed comparative results between our TGA-based algorithms (MA-NTGA and MA-ETGA) and state-of-the-art methods on the three benchmark sets, respectively. For the CVRP and VRPTW, the BKS values are obtained from the CVRPLIB repository (<http://vrp.galgos.inf.puc-rio.br/>) as of December 25, 2025. For the CVRP, we use results from HGS-2012 [37] and HGS-CVRP [14]. For the VRPTW, with the objective of minimizing the total travel distance, we report results from the DIMACS competition, including both the official DIMACS reference results and the champion team’s algorithm, HGS-DIMACS [38]. For the VRPSPDTW, we report the best results from the state-of-the-art MA-FIRD method [31]. Our MA-NTGA and MA-ETGA results are derived from the best solutions obtained in the experiments reported in Section A3.

Each table reports the instance name (*Instance*), the number of customers (N_C), the best-known solution (BKS), the best objective value (f^*) achieved

by each reference algorithm, and the corresponding gap ($\text{Gap}(\%)$) relative to the BKS. The time column (t) follows the same definition and settings as in Section A3.

Table A2

Summary of key notation.

Notation	Description
Problem Description	
$\mathcal{G} = (\mathcal{V}, \mathcal{E})$	Complete graph with nodes \mathcal{V} and edges \mathcal{E}
$\mathcal{V} = \{v_0, v_1, \dots, v_{N_C}\}$	Nodes: depot v_0 and customers $\{v_1, \dots, v_{N_C}\}$
$\mathcal{E} = \{e_{ij} \mid v_i, v_j \in \mathcal{V}\}$	Set of edges connecting nodes v_i and v_j
N_C	Number of customers
d_i, p_i	Delivery and pickup demands of node v_i
e_i, l_i, s_i	Earliest time, latest time, and service time of node v_i
$\mathcal{C} = (c_{ij}), \mathcal{T} = (t_{ij})$	Travel distance matrix and time matrix
c_{ij}, t_{ij}	Travel distance and time between nodes v_i and v_j
Q	Vehicle capacity
Solution Representation	
S	Solution consisting of a set of routes $\{R_1, \dots, R_M\}$
M	Number of vehicles
R_i	Route i , a sequence of nodes
\mathcal{L}_i	Number of customers in route R_i
$ R_i $	Length of route R_i (including depots)
$n_{i,j}$	The j -th node in route R_i
$q_{n_{i,j}}$	Vehicle load after visiting node $n_{i,j}$
$a_{n_{i,j}}, w_{n_{i,j}}$	Arrival time and waiting time at node $n_{i,j}$
$f(S)$	Objective value of solution S
$D(S)$	Total travel distance of solution S
μ_1, μ_2	Weights in the objective function
Sequence Concatenation-based Move Evaluation	
$\sigma, \sigma^0, \sigma_1, \sigma_2$	Route subsequences
\oplus	Sequence concatenation operator
$D(\sigma)$	Travel distance of subsequence σ
$L_I(\sigma), L_O(\sigma), L_M(\sigma)$	Load attributes of subsequence σ
$T_D(\sigma), T_E(\sigma), T_L(\sigma), T_V(\sigma)$	Time window attributes of subsequence σ
$\Delta_t, \Delta_w, \Delta_v$	Intermediate variables for time-window attribute calculations
Tensor-based GPU Acceleration	
$\mathbf{T}_s \in \mathbb{R}^{I \times J \times K \times K}$	Tensor with dimensions $I \times J \times K \times K$
L	Feasible length of the sequence attribute tensors in the route-based extraction
Q	Number of valid nodes in node-based extraction ($Q = M + N_C$)
E	Number of valid node pairs in edge-based extraction
\mathbf{D}	Travel distance attribute tensor
$\mathbf{L}_I, \mathbf{L}_O, \mathbf{L}_M$	Load attribute tensors
$\mathbf{T}_D, \mathbf{T}_E, \mathbf{T}_L, \mathbf{T}_V$	Time window attribute tensors
$\mathbf{I}_S, \mathbf{I}_E$	First and last node index tensors
\mathbf{B}	Boolean mask tensor
\mathbf{C}, \mathbf{T}	Travel distance and time tensors corresponding to \mathcal{C} and \mathcal{T}
S_h, S_m, S_t, S_r, S_d	Route subsequences
$\mathbf{S}_h, \mathbf{S}_m, \mathbf{S}_t, \mathbf{S}_p, \mathbf{S}_q$	Sequence attribute tensors
$\mathbf{S}_{r1}, \mathbf{S}_{r2}, \mathbf{S}_{m1}, \mathbf{S}_{m2}, \mathbf{S}_{d1}, \mathbf{S}_{d2}$	Auxiliary sequence attribute tensors
N, N_1, N_2	Sequence lengths in relocate, swap, and 3-Seq extractions
$\mathbf{P} = \{\mathbf{P}_r, \mathbf{P}_\pi\}$	Positional tensors
\mathbf{M}	Mask tensor for valid node pairs under neighborhood reduction
$\mathbf{E} = \{\mathbf{E}_i, \mathbf{E}_j\}$	Edge index tensors
$\Delta \mathbf{D}, \Delta \mathbf{T}_V, \Delta \mathbf{L}_V$	Attribute delta tensors
\mathcal{F}	Evaluation function
\mathbf{F}	Scoring tensor
F_{\min}	Minimum score value in \mathbf{F}
α^*	Indices of the best move (argmin of \mathbf{F})
ζ	Best move decoded from α^*
Algorithm and Experiments	
μ	Population size
θ	Granularity threshold for neighborhood reduction
γ_s	Speedup ratio

Table A3

Comparative results on the 100 X benchmark instances for MA-N, MA-E, MA-NTGA, and MA-ETGA.

Instance	N_C	t	MA-N				MA-E				MA-NTGA				MA-ETGA			
			M	f^*	f	Gap(%)	M	f^*	f	Gap(%)	M	f^*	f	Gap(%)	M	f^*	f	Gap(%)
X-n101-k25	100	240.0	26.0	27591.0	27597.8	26.0	27591.0	27603.4	0.02	26.0	27591.0	27605.0	0.03	26.0	27591.0	27599.8	0.01	
X-n106-k14	105	252.0	14.0	26381.0	26481.4	14.0	26392.0	26435.4	-0.17	14.0	26403.0	26464.2	-0.06	14.0	26403.0	26464.6	-0.06	
X-n110-k13	109	261.6	13.0	14971.0	14988.9	13.0	14971.0	14992.6	0.02	13.0	14971.0	14999.8	0.07	13.0	14971.0	15001.4	0.08	
X-n115-k10	114	273.6	10.0	12747.0	12758.1	10.0	12747.0	12773.9	0.12	10.0	12747.0	12751.7	-0.05	10.0	12747.0	12754.8	-0.03	
X-n120-k6	119	285.6	6.0	13332.0	13397.8	6.0	13332.0	13380.5	-0.13	6.0	13332.0	13373.8	-0.18	6.0	13332.0	13363.6	-0.26	
X-n125-k30	124	297.6	30.0	55662.0	55641.0	30.0	55551.0	55636.3	-0.01	30.0	55626.0	55721.0	0.14	30.0	55600.0	55682.4	0.07	
X-n129-k18	128	307.2	18.0	29015.0	29259.0	18.0	29033.0	29138.5	-0.41	18.0	29012.0	29361.4	0.35	18.0	29020.0	29247.7	-0.04	
X-n134-k13	133	319.2	13.0	10918.0	10955.8	13.0	10934.0	10955.9	0.00	13.0	10920.0	10953.1	-0.02	13.0	10918.0	10972.8	0.15	
X-n139-k10	138	331.2	10.1	13590.0	13604.4	10.2	13590.0	13612.9	0.06	10.2	13590.0	13610.8	0.05	10.1	13590.0	13603.9	0.00	
X-n143-k7	142	340.8	7.0	15700.0	15757.8	7.0	15740.0	15813.4	0.35	7.0	15726.0	15765.4	0.05	7.0	15740.0	15814.7	0.36	
X-n148-k46	147	352.8	46.8	43449.0	43550.5	46.5	43541.0	43674.3	0.28	46.4	43449.0	43614.4	0.15	46.7	43461.0	43693.4	0.33	
X-n153-k22	152	364.8	23.0	21234.0	21315.5	23.0	21250.0	21284.4	-0.15	23.0	21262.0	21326.5	0.05	23.1	21282.0	21382.2	-0.31	
X-n157-k13	156	374.4	13.0	16876.0	16921.2	13.0	16888.0	16926.9	0.03	13.0	16876.0	16917.5	-0.02	13.0	16876.0	16906.1	0.09	
X-n162-k11	161	386.4	11.0	14138.0	14164.4	11.0	14138.0	14191.9	0.19	11.0	14138.0	14161.7	-0.02	11.0	14147.0	14179.9	0.11	
X-n167-k10	166	398.4	10.0	20583.0	20720.4	10.0	20583.0	20687.8	-0.16	10.0	20583.0	20709.2	-0.05	10.0	20557.0	20782.7	0.30	
X-n172-k51	171	410.4	53.0	45705.0	45835.7	53.0	45629.0	45783.0	-0.11	53.1	45610.0	45739.7	-0.21	53.0	45616.0	45735.5	-0.22	
X-n176-k26	175	420.0	26.0	47843.0	48065.6	26.0	47840.0	48015.3	-0.10	26.0	47915.0	48033.9	-0.07	26.0	47899.0	48060.4	-0.01	
X-n181-k23	180	432.0	23.0	25593.0	25677.1	23.0	25597.0	25664.2	-0.05	23.0	25644.0	25685.4	0.03	23.0	25593.0	25667.7	-0.04	
X-n186-k15	185	444.0	15.0	24173.0	24311.2	15.0	24196.0	24315.6	-0.02	15.0	24154.0	24354.5	0.18	15.0	24180.0	24300.9	-0.04	
X-n190-k8	189	453.6	8.0	16995.0	17130.6	8.0	17050.0	17178.0	0.28	8.0	17057.0	17121.1	-0.06	8.0	17015.0	17116.5	-0.08	
X-n195-k51	194	465.6	52.4	44321.0	44502.5	52.5	44392.0	44557.4	0.12	52.7	44361.0	44447.0	-0.12	52.8	44313.0	44440.5	-0.14	
X-n200-k36	199	477.6	36.0	58674.0	58796.4	36.0	58669.0	58733.4	-0.11	36.0	58730.0	58825.1	0.05	36.0	58711.0	58805.8	0.02	
X-n204-k19	203	487.2	19.0	19700.0	19741.2	19.0	19598.0	19720.1	-0.11	19.0	19610.0	19707.8	-0.17	19.0	19570.0	19699.5	-0.21	
X-n209-k16	208	499.2	16.0	30673.0	30847.6	16.0	30730.0	30850.4	0.01	16.0	30736.0	30928.4	0.26	16.0	30756.0	30910.5	0.20	
X-n214-k11	213	511.2	11.0	11030.0	11067.6	11.0	10886.0	10974.4	-0.84	11.0	10927.0	11020.9	-0.42	11.0	11005.0	11055.8	-0.11	
X-n219-k73	218	523.2	73.0	117616.0	117693.2	73.0	117598.0	117695.0	0.00	73.0	117624.0	117706.7	0.01	73.0	117616.0	117716.0	0.02	
X-n223-k34	222	532.8	34.0	40665.0	40821.8	34.0	40600.0	40777.3	-0.11	34.0	40587.0	40803.0	-0.05	34.0	40627.0	40858.8	-0.09	
X-n228-k23	227	544.8	23.0	25865.0	26065.8	23.0	25843.0	25917.5	-0.57	23.0	25870.0	26030.3	-0.14	23.0	25881.0	25954.1	-0.43	
X-n233-k16	232	556.8	17.0	19341.0	19491.9	17.0	19357.0	19498.3	0.03	17.0	19333.0	19405.2	-0.44	17.0	19337.0	19426.2	-0.34	
X-n237-k14	236	566.4	14.0	27320.0	27538.1	14.0	27186.0	27515.0	-0.08	14.0	27318.0	27496.0	-0.15	14.0	27346.0	27495.8	-0.15	
X-n242-k48	241	578.4	48.0	83334.0	83566.8	48.0	83106.0	83384.3	-0.22	48.0	83443.0	83510.0	-0.07	48.0	83319.0	83714.8	0.18	
X-n247-k50	246	590.4	51.0	37440.0	37510.1	51.0	37392.0	37491.4	-0.05	51.0	37387.0	37435.9	-0.20	51.5	37387.0	37592.8	0.22	
X-n251-k28	250	600.0	28.0	39008.0	39171.9	28.0	38927.0	39013.3	-0.40	28.0	38940.0	39099.1	-0.19	28.0	38966.0	39156.0	-0.04	
X-n256-k16	255	612.0	17.0	18984.0	19073.2	16.1	18915.0	18975.9	-0.51	16.9	18920.0	18939.9	-0.17	16.8	18929.0	19028.7	-0.23	
X-n261-k13	260	624.0	13.0	26805.0	27045.8	13.0	26683.0	26896.1	-0.55	13.0	26752.0	26895.6	-0.56	13.0	26672.0	26982.8	-0.23	
X-n266-k58	265	636.0	58.3	76281.0	76450.2	58.7	76204.0	76966.4	0.68	58.4	75942.0	76170.8	-0.37	58.5	76109.0	76392.1	-0.08	
X-n270-k35	269	645.6	36.0	35888.0	35993.4	36.0	36047.0	36215.1	0.62	36.0	35525.0	35597.1	-1.10	36.0	35543.0	35690.4	-0.84	
X-n275-k28	274	657.6	28.0	21480.0	21545.8	28.0	21394.0	21515.3	-0.14	28.0	21452.0	21506.3	-0.18	28.0	21412.0	21502.2	-0.20	
X-n280-k17	279	669.6	17.0	33738.0	33990.0	17.0	33653.0	33815.1	-0.34	17.0	33656.0	34022.0	0.09	17.0	33689.0	33912.8	-0.23	
X-n284-k15	283	679.2	15.0	20723.0	20988.4	15.0	20623.0	20785.6	-0.97	15.0	20632.0	20938.1	-0.24	15.0	20724.0	20998.9	0.05	
X-n289-k60	288	691.2	61.6	97395.0	97898.3	61.6	97156.0	97593.3	-0.31	61.4	96330.0	96598.7	-1.33	61.5	96271.0	96690.6	-1.23	
X-n294-k50	293	703.2	51.0	47910.0	48202.0	51.0	47988.0	48283.3	0.17	51.0	47421.0	47559.1	-1.33	51.0	47531.0	47612.6	-1.22	
X-n298-k31	297	712.8	31.0	34661.0	34825.1	31.0	34407.0	34691.1	-0.38	31.0	34416.0	34770.6	-0.16	31.0	34552.0	34769.6	-0.16	
X-n303-k21	302	724.8	21.0	21943.0	22009.2	21.0	21931.0	22021.3	0.05	21.0	21868.0	21980.1	-0.13	21.0	21951.0	22000.3	-0.04	
X-n308-k13	307	736.8	13.0	25993.0	26304.3	13.0	25993.0	26194.1	-0.42	13.0	26044.0	26213.5	-0.35	13.0	25924.0	26168.4	-0.52	
X-n313-k71	312	748.8	72.2	96003.0	96299.8	72.6	95676.0	96004.5	-0.31	72.6	94891.0	95104.5	-1.24	72.9	94800.0	95212.2	-1.13	
X-n317-k53	316	758.4	53.0	78521.0	78568.8	53.0	78478.0	78517.6	-0.07	53.0	78515.0	78562.8	-0.01	53.0	78479.0	78575.4	0.01	
X-n322-k28	321	770.4	28.5	30527.0	30639.7	28.0	30075.0	30155.7	-1.58	28.1	30082.0	30185.0	-1.48	28.3	30097.0	30219.5	-1.37	
X-n327-k20	326	782.4	20.0	27910.0	28039.1	20.0	27657.0	27895.3	-0.51	20.0	27738.0	27953.4	-0.31	20.0	27850.0	27997.3	-0.15	
X-n331-k15	330	792.0	15.0	31398.0	31642.5	15.0	31278.0	31541.3	-0.32	15.0	31408.0	31650.0	0.02	15.0	31340.0	31532.3	-0.35	
X-n336-k84	335	804.0	85.7	142668.0	143056.7	85.5	142707.0	143265.8	0.15	86.1	140544.0	140962.2	-1.46	86.2	140645.0	141100.6	-1.37	
X-n344-k43	343	823.2	43.4	42823.0	43094.0	43.0	42501.0	42660.1	-1.01	43.2	42468.0	42617.4	-1.11	43.4	42509.0	42710.4	-0.89	
X-n351-k40	350	840.0	40.0	26973.0	27065.4	41.0	26995.0	27162.8	0.36	41.0	26247.0	26376.9	-2.54	41.0	26381.0	26471.1	-2.20	
X-n359-k29	358	859.2	29.0	52268.0	52568.2	29.0	51951.0	52352.6	-0.41	29.0	52090.0	52325.9	-0.46	29.0	52178.0	52405.3	-0.31	
X-n367-k17	366	878.4	17.0	23100.0	23268.3	17.0	22968.0	23215.5	-0.23	17.0	22986.0	23189.4	-0.34	17.0	22902.0	23172.0	-0.41	
X-n376-k94	375	900.0	94.0	147893.0	148041.4	94.0	147821.0	148159.3	0.08	94.0	147838.0	147943.0	-0.07	94.0	147873.0	147994.2	-0.03	
X-n384-k52	383	919.2	53.2	67889.0	68359.2	53.0	67978.0	68673.2	0.46	53.0	66906.0	67111.2	-1.83	53.0	67103.0	67321.1	-1.52	
X-n393-k38	392	940.8	38.0	38838.0	39007.4	38.0	38494.0	38757.8	-0.64	38.0	38596.0	38766.0	-0.62	38.0	38620.0	38799.0	-0.53	
X-n401-k29	400	960.0	29.0	66754.0	66913.8	29.0	66527.0	66865.2	-0.07	29.0	66671.0	66840.6	-0.11	29.0	66511.0	66713.8	-0.30	
X-n411-k19	410	984.0	19.0	20003.0	20165.9	19.0	19943.0	20041.1	-0.62	19.0	19914.0	20095.3	-0.35	19.0	20022.0	20137.7	-0.14	
X-n420-k130	419	1005.6	130.1	109131.0	109670.8	130.0	108436.0	108644.0	-0.92	130.0	108294.0	108639.6	-0.94	130.0	108558.0	108753.5	-0.84	
X-n429-k61	428	1027.2	61.8	67802.0	67995.3	61.4	67022.0	67817.0	-0.26	61.8	66112							

Table A4

Comparative results on the 100 X benchmark instances for MA-N, MA-E, MA-NTGA, and MA-ETGA (continued).

Instance	N_C	t	MA-N			MA-E				MA-NTGA				MA-ETGA			
			M	f^*	f	M	f^*	f	Gap(%)	M	f^*	f	Gap(%)	M	f^*	f	Gap(%)
X-n613-k62	612	1468.8	62.0	62921.0	63335.5	62.0	61330.0	62086.2	-1.97	62.0	60571.0	60698.4	-4.16	62.0	60687.0	60861.2	-3.91
X-n627-k43	626	1502.4	43.5	64169.0	64712.4	43.3	63621.0	64700.9	-0.02	43.0	63015.0	63320.0	-2.15	43.0	63096.0	63305.3	-2.17
X-n641-k35	640	1536.0	35.0	65633.0	65826.2	35.0	64905.0	65975.3	0.23	35.0	64516.0	64847.8	-1.49	35.0	64684.0	64848.6	-1.49
X-n655-k131	654	1569.6	131.0	107273.0	107394.4	131.0	107343.0	107908.7	0.48	131.0	107248.0	107338.8	-0.05	131.0	107269.0	107354.4	-0.04
X-n670-k130	669	1605.6	133.3	149871.0	150288.7	133.7	148928.0	149451.6	-0.56	133.0	147491.0	147731.1	-1.70	134.8	147803.0	148602.4	-1.12
X-n685-k75	684	1641.6	75.2	72087.0	72821.3	75.6	70656.0	71193.7	-2.24	75.6	69319.0	69634.2	-4.38	75.9	69510.0	69859.7	-4.07
X-n701-k44	700	1680.0	44.0	84492.0	84977.4	44.0	83091.0	85201.1	0.26	44.0	83308.0	83691.9	-1.51	44.0	83523.0	83884.9	-1.29
X-n716-k35	715	1716.0	35.0	45189.0	45474.4	35.0	44554.0	45146.1	-0.72	35.0	44188.0	44385.2	-2.40	35.0	44119.0	44416.6	-2.33
X-n733-k159	732	1756.8	159.0	144775.0	146324.9	159.5	139958.0	141074.4	-3.59	160.0	137896.0	138373.5	-5.43	160.0	138426.0	138629.7	-5.26
X-n749-k98	748	1795.2	98.0	81196.0	82731.1	98.2	80324.0	81056.9	-2.02	98.4	78836.0	79020.1	-4.49	98.8	78970.0	79310.6	-4.13
X-n766-k71	765	1836.0	71.0	121067.0	122634.3	71.0	118294.0	119175.5	-2.82	71.0	117135.0	117724.3	-4.00	71.0	116629.0	117443.4	-4.23
X-n783-k48	782	1876.8	48.0	75520.0	76614.0	48.0	76064.0	76842.8	0.30	48.0	73679.0	74168.9	-3.19	48.0	73718.0	74257.3	-3.08
X-n801-k40	800	1920.0	40.0	75041.0	75537.1	40.0	74504.0	75187.5	-0.46	40.0	74533.0	74693.4	-1.12	40.0	74639.0	74936.4	-0.80
X-n819-k171	818	1963.2	174.2	163641.0	164406.7	173.6	163549.0	164922.8	0.31	172.5	159878.0	160581.7	-2.33	173.0	161000.0	161310.7	-1.88
X-n837-k142	836	2006.4	143.7	202047.0	203973.9	143.3	200161.0	201612.7	-1.16	142.6	196109.0	196812.1	-3.51	142.9	196834.0	197951.2	-2.95
X-n856-k95	855	2052.0	95.0	90428.0	90581.7	95.0	90042.0	91351.7	0.85	95.0	89939.0	90175.2	-0.45	95.0	90023.0	90185.2	-0.44
X-n876-k59	875	2100.0	59.0	102264.0	103002.7	59.0	101369.0	103433.1	0.42	59.0	100718.0	101072.3	-1.87	59.0	100931.0	101196.8	-1.75
X-n895-k37	894	2145.6	37.3	57758.0	58860.9	37.9	58238.0	58654.9	-0.35	38.0	55170.0	55486.2	-5.73	38.0	55189.0	55592.3	-5.55
X-n916-k207	915	2196.0	208.7	342404.0	343969.5	207.0	336363.0	337671.2	-1.83	208.0	332728.0	333422.3	-3.07	208.0	334515.0	335608.6	-2.43
X-n936-k151	935	2244.0	161.0	138669.0	139042.5	160.9	136899.0	137666.4	-0.99	160.0	134944.0	135214.0	-2.75	160.8	135026.0	135594.0	-2.48
X-n957-k87	956	2294.4	87.0	87218.0	87386.7	87.0	87100.0	88270.2	1.01	87.0	86748.0	86950.7	-0.50	87.0	86780.0	87044.0	-0.39
X-n979-k58	978	2347.2	58.0	122751.0	123705.7	58.1	122219.0	123003.6	-0.57	58.0	120156.0	120769.3	-2.37	58.0	120106.0	120659.8	-2.46
X-n1001-k43	1000	2400.0	43.0	76258.0	77086.4	43.0	74715.0	76189.8	-1.16	43.0	74271.0	74704.4	-3.09	43.0	74212.0	74612.7	-3.21
MEAN	-	989.3	50.8	64611.6	64962.8	50.8	64182.9	64607.9	-0.38	50.8	63716.1	63926.8	-1.05	50.8	63810.9	64043.9	-0.94

Table A5

Comparative results on the 90 GH benchmark instances for MA-N, MA-E, MA-NTGA, and MA-ETGA.

Instance	N_C	t	MA-N			MA-E				MA-NTGA				MA-ETGA			
			M	f^*	f	M	f^*	f	Gap(%)	M	f^*	f	Gap(%)	M	f^*	f	Gap(%)
C1.2.1	200	1800.0	20.0	2698.6	2698.6	20.0	2698.6	2698.6	0.00	20.0	2698.6	2698.6	0.00	20.0	2698.6	2698.6	0.00
C1.2.5	200	1800.0	20.0	2694.9	2694.9	20.0	2694.9	2694.9	0.00	20.0	2694.9	2694.9	0.00	20.0	2694.9	2694.9	0.00
C1.2.10	200	1800.0	19.0	2624.7	2625.6	19.0	2624.7	2625.6	0.04	19.0	2624.7	2625.6	0.00	19.0	2624.7	2625.6	0.00
C2.2.1	200	1800.0	6.9	1922.1	1922.3	7.0	1922.1	1922.1	-0.01	7.0	1922.1	1922.3	0.00	7.0	1922.1	1922.1	-0.01
C2.2.5	200	1800.0	7.0	1869.6	1869.6	7.0	1869.6	1869.6	0.00	6.9	1869.6	1869.9	0.01	7.0	1869.6	1869.6	0.00
C2.2.10	200	1800.0	6.9	1791.2	1793.8	7.0	1791.2	1792.0	-0.10	6.9	1791.2	1792.6	-0.07	7.0	1791.2	1792.1	-0.09
R1.2.1	200	1800.0	23.0	4667.2	4669.1	23.0	4667.2	4667.4	-0.03	23.0	4667.2	4672.6	0.08	22.9	4667.2	4668.1	-0.02
R1.2.5	200	1800.0	20.0	4053.2	4053.9	20.0	4053.2	4054.4	0.01	20.0	4053.2	4054.3	0.01	20.0	4053.2	4053.7	-0.01
R1.2.10	200	1800.0	18.0	3293.1	3300.6	18.0	3293.1	3298.7	-0.06	18.0	3293.1	3300.7	0.00	18.0	3293.8	3303.4	0.08
R2.2.1	200	1800.0	9.6	3482.0	3551.1	9.1	3497.1	3573.3	0.63	9.4	3507.5	3566.2	0.43	10.1	3478.4	3516.3	-0.98
R2.2.5	200	1800.0	7.8	3065.2	3072.0	7.2	3061.1	3087.2	0.49	7.6	3069.1	3086.8	0.48	7.2	3063.6	3089.4	0.57
R2.2.10	200	1800.0	5.4	2556.7	2608.9	5.8	2555.7	2599.1	-0.37	6.0	2557.8	2589.4	-0.75	6.0	2561.1	2592.9	-0.61
RC1.2.1	200	1800.0	20.0	3516.9	3518.2	19.8	3516.9	3518.9	0.02	20.0	3516.9	3517.4	-0.02	19.9	3516.9	3517.0	-0.03
RC1.2.5	200	1800.0	19.0	3325.6	3328.6	19.0	3326.3	3328.1	-0.01	19.0	3325.6	3327.5	-0.03	19.0	3326.3	3328.2	-0.01
RC1.2.10	200	1800.0	18.6	2997.6	3010.9	18.4	2996.5	3008.2	-0.09	18.3	2993.8	3003.6	-0.24	18.3	2996.9	3005.1	-0.19
RC2.2.1	200	1800.0	8.8	2797.4	2806.7	8.7	2799.0	2806.9	0.01	9.0	2797.4	2806.2	-0.02	9.1	2797.4	2801.3	-0.19
RC2.2.5	200	1800.0	7.2	2491.4	2503.7	7.1	2492.1	2502.3	-0.05	7.2	2491.4	2503.7	0.00	7.2	2492.1	2500.5	-0.12
RC2.2.10	200	1800.0	5.0	1989.3	2005.1	4.8	1992.1	2004.4	-0.03	5.0	2000.0	2005.6	0.03	4.9	1997.0	2007.9	0.14
C1.4.1	400	3600.0	40.0	7138.8	7138.8	40.0	7138.8	7138.8	0.00	40.0	7138.8	7138.8	0.00	40.0	7138.8	7138.8	0.00
C1.4.5	400	3600.0	40.0	7138.8	7138.8	40.0	7138.8	7138.8	0.00	40.0	7138.8	7138.8	0.00	40.0	7138.8	7138.8	0.00
C1.4.10	400	3600.0	37.0	6830.1	6835.6	37.0	6826.7	6828.2	-0.11	37.0	6825.7	6826.9	-0.13	37.0	6826.5	6827.9	-0.11
C2.4.1	400	3600.0	12.0	4100.3	4100.3	12.0	4100.3	4100.3	0.00	12.0	4100.3	4100.3	0.00	12.0	4100.3	4100.3	0.00
C2.4.5	400	3600.0	12.0	3923.2	3926.3	12.0	3927.5	3927.5	0.03	12.0	3927.5	3927.5	0.03	12.0	3923.2	3924.9	-0.03
C2.4.10	400	3600.0	12.1	3665.2	3675.4	12.1	3665.1	3671.8	-0.10	12.0	3665.1	3675.1	-0.01	12.0	3665.1	3669.9	-0.15
R1.4.1	400	3600.0	41.6	10339.5	10370.7	41.3	10331.9	10354.2	-0.16	41.3	10313.8	10323.9	-0.45	41.5	10337.6	10356.9	-0.13
R1.4.5	400	3600.0	37.9	9221.0	9255.6	37.9	9204.4	9223.3	-0.35	38.0	9208.7	9220.9	-0.37	37.6	9198.4	9216.7	-0.42
R1.4.10	400	3600.0	37.0	8231.6	8267.4	37.0	8151.2	8206.5	-0.74	36.9	8109.5	8155.2	-1.36	37.0	8138.7	8171.4	-1.16
R2.4.1	400	3600.0	17.2	7556.1	7679.3	17.7	7525.2	7601.2	-1.02	17.1	7559.7	7661.0	-0.24	18.1	7526.8	7547.5	-1.72
R2.4.5	400	3600.0	12.6	6580.0	6658.2	12.4	6578.5	6685.2	0.41	12.4	6568.1	6678.4	0.30	12.5	6577.1	6661.9	0.06
R2.4.10	400	3600.0	10.3	5707.6	5750.2	9.8	5699.4	5752.7	0.04	10.2	5690.2	5738.3	-0.21	10.1	5694.0	5737.6	-0.22
RC1.4.1	400	3600.0	37.0	8568.9	8605.2	37.0	8535.2	8559.1	-0.54	37.6	8524.0	8580.0	-0.29	37.0	8527.2	8557.1	-0.56
RC1.4.5	400	3600.0	37.0	8255.2	8292.9	37.0	8206.1	8236.3	-0.68	37.0	8196.4	8211.3	-0.98	37.0	8206.7	8226.8	-0.80
RC1.4.10	400	3600.0	36.8	7719.9	7795.8	36.8	7670.0	7730.9	-0.83	36.8	7634.5	7697.4	-1.26	36.5	7634.0	7686.3	-1.40
RC2.4.1	400	3600.0	16.1	6153.7	6173.7	15.8	6147.3	6171.4	-0.04	16.4	6156.2	6172.8	-0.01	15.9	6148.7	6175.4	0.03
RC2.4.5	400	3600.0	13.0	5402.9	5419.0	13.0	5401.5	5418.6	-0.01	13.3	5400.1	5418.7	-0.01	13.0	5394.7	5408.0	-0.20
RC2.4.10	400	3600.0	8.2	4284.4	4334.3	8.1	4276.5	4302.1	-0.74	8.5	4266.6	4295.4	-0.90	8.5	4261.6	4300.0	-0.79
C1.6.1	600	3600.0	60.0	14076.6	14076.6	60.0	14076.6	14076.6	0.00	60.0	14076.6	140					

Table A6

Comparative results on the 90 *GH* benchmark instances for MA-N, MA-E, MA-NTGA, and MA-ETGA (continued).

Instance	N_C	t	MA-N				MA-E				MA-NTGA				MA-ETGA			
			M	f^*	f	Gap(%)	M	f^*	f	Gap(%)	M	f^*	f	Gap(%)	M	f^*	f	Gap(%)
			R1_6.1	600	3600.0	61.2	21711.0	21858.9	59.1	21377.2	21515.9	-1.57	58.1	21314.5	21352.3	-2.32	58.2	21315.5
R1_6.5	600	3600.0	56.6	19884.8	19992.1	56.2	19552.0	19641.4	-1.75	56.0	19435.8	19523.9	-2.34	56.0	19463.8	19545.8	-2.23	
R1_6.10	600	3600.0	55.2	18226.7	18355.5	55.0	17958.7	18040.4	-1.72	55.0	17711.0	17799.5	-3.03	55.0	17795.1	17861.1	-2.69	
R2_6.1	600	3600.0	20.0	15654.4	16012.2	21.4	15259.8	15595.6	-2.60	21.4	15274.1	15693.4	-1.99	23.4	15194.9	15418.9	-3.71	
R2_6.5	600	3600.0	15.7	14519.5	14786.5	17.3	13962.7	14226.6	-3.79	18.2	13895.0	14202.2	-4.51	18.3	13926.5	14150.4	-4.30	
R2_6.10	600	3600.0	13.0	12465.8	12633.6	13.1	12024.2	12245.4	-3.07	13.8	12010.4	12084.8	-4.34	13.6	11988.6	12090.3	-4.30	
RC1_6.1	600	3600.0	57.2	17448.6	17523.0	56.8	17179.5	17215.4	-1.76	56.4	17037.9	17111.6	-2.35	56.7	17069.3	17113.1	-2.34	
RC1_6.5	600	3600.0	56.7	17123.0	17237.3	56.3	16872.9	16916.0	-1.86	56.0	16682.9	16744.9	-2.86	56.1	16696.2	16755.3	-2.80	
RC1_6.10	600	3600.0	55.8	16394.2	16535.9	55.6	16043.1	16160.4	-2.27	55.7	15870.0	15943.1	-3.58	55.6	15915.0	16018.5	-3.13	
RC2_6.1	600	3600.0	21.5	12118.8	12205.5	21.8	11982.7	12037.9	-1.37	22.1	12005.7	12062.6	-1.17	22.0	11986.7	12047.7	-1.29	
RC2_6.5	600	3600.0	19.6	11290.7	11419.1	19.1	11114.8	11192.7	-1.98	19.4	11111.9	11188.1	-2.02	19.3	11109.5	11156.0	-2.30	
RC2_6.10	600	3600.0	12.6	9219.8	9394.8	12.6	9040.2	9114.0	-2.99	12.5	9028.3	9075.7	-3.40	12.5	9036.1	9077.4	-3.38	
CL_8.1	800	3600.0	80.0	25156.9	25156.9	80.0	25156.9	25157.3	0.00	80.0	25156.9	25156.9	0.00	80.0	25156.9	25157.3	0.00	
CL_8.5	800	3600.0	80.0	25138.6	25138.7	80.0	25138.6	25139.3	0.00	80.0	25138.6	25138.6	0.00	80.0	25138.6	25139.4	0.00	
CL_8.10	800	3600.0	73.5	24908.6	25203.7	73.0	24251.3	24376.8	-3.28	73.0	24094.3	24141.2	-4.22	73.0	24091.5	24152.7	-4.17	
CL_8.1	800	3600.0	24.0	11631.9	11632.6	24.0	11631.9	11634.1	0.01	24.0	11631.9	11632.0	0.00	24.0	11631.9	11634.5	0.02	
C2_8.5	800	3600.0	24.0	11399.6	11411.2	24.0	11395.6	11402.8	-0.07	24.0	11395.6	11398.0	-0.12	24.0	11395.6	11399.2	-0.11	
C2_8.10	800	3600.0	24.3	11103.0	11310.4	24.0	10961.3	10994.4	-2.79	24.0	10950.2	10989.0	-2.84	24.0	10957.6	10972.2	-2.99	
R1_8.1	800	3600.0	81.7	37482.8	37712.0	79.9	37038.5	37171.0	-1.43	79.7	36641.8	36720.4	-2.63	79.1	36704.2	36847.0	-2.29	
R1_8.5	800	3600.0	75.3	34841.2	34988.0	74.5	34243.4	34433.5	-1.58	74.0	33815.4	33937.0	-3.00	74.2	33849.3	34060.3	-2.65	
R1_8.10	800	3600.0	72.9	32847.2	32979.8	73.2	31919.5	32049.4	-2.82	73.0	31436.6	31594.0	-4.20	73.0	31573.6	31738.5	-3.76	
R2_8.1	800	3600.0	21.8	26502.0	26865.9	25.1	25228.8	25575.5	-4.80	26.5	25237.3	25426.9	-5.36	25.7	25129.0	25405.7	-5.41	
R2_8.5	800	3600.0	17.5	24738.1	24984.2	21.6	23131.2	23708.4	-5.11	23.2	23026.9	23211.1	-7.10	24.0	22929.3	23132.6	-7.44	
R2_8.10	800	3600.0	16.0	21497.2	21696.9	18.3	20638.9	20959.2	-3.40	19.3	20154.0	20274.6	-6.55	18.3	20250.8	20389.4	-6.03	
RC1_8.1	800	3600.0	75.7	31037.5	31241.0	74.9	30503.6	30670.5	-1.83	74.6	30186.5	30325.2	-2.93	74.3	30193.5	30382.3	-2.75	
RC1_8.5	800	3600.0	74.8	30316.2	30506.7	74.2	29794.4	30042.0	-1.52	74.0	29514.3	29578.7	-3.04	74.0	29556.2	29644.5	-2.83	
RC1_8.10	800	3600.0	73.3	29634.7	30175.1	73.0	29136.8	29295.5	-2.92	73.0	28564.8	28644.9	-5.07	73.1	28786.5	28876.6	-4.30	
RC2_8.1	800	3600.0	26.0	19796.1	19931.0	25.4	19263.7	19338.9	-2.97	25.6	19279.2	19341.9	-2.96	25.9	19239.9	19308.8	-3.12	
RC2_8.5	800	3600.0	23.0	18175.5	18316.8	22.7	17609.3	17714.7	-3.29	22.6	17540.8	17611.1	-3.85	22.5	17595.1	17666.8	-3.55	
RC2_8.10	800	3600.0	16.4	15182.1	15356.6	16.5	14684.0	14826.1	-3.45	16.0	14470.6	14531.7	-5.37	16.0	14478.0	14533.1	-5.36	
C1_10.1	1000	7200.0	100.0	42444.8	42444.9	100.0	42445.8	42447.2	0.01	100.0	42444.8	42444.8	0.00	100.0	42444.8	42446.2	0.00	
C1_10.5	1000	7200.0	100.0	42435.5	42436.1	100.0	42435.5	42437.0	0.00	100.0	42434.8	42435.7	0.00	100.0	42435.5	42436.7	0.00	
C1_10.10	1000	7200.0	91.7	41332.2	41790.0	91.7	40425.3	40645.7	-2.74	90.9	40030.1	40253.0	-3.68	91.2	40058.6	40231.0	-3.73	
C2_10.1	1000	7200.0	30.0	16841.1	16841.1	30.0	16841.1	16841.1	0.00	30.0	16841.1	16842.2	0.01	30.0	16841.1	16841.3	0.00	
C2_10.5	1000	7200.0	30.0	16532.2	16553.7	30.0	16525.6	16538.2	-0.09	30.0	16521.9	16533.2	-0.12	30.0	16522.9	16538.5	-0.09	
C2_10.10	1000	7200.0	30.0	15965.0	16158.4	30.0	15747.6	15790.8	-2.28	30.0	15773.0	15786.3	-2.30	30.0	15750.8	15775.0	-2.37	
R1_10.1	1000	7200.0	98.1	55067.3	55329.0	95.9	53996.7	54106.9	-2.21	94.9	53488.9	53610.4	-3.11	94.7	53522.0	53634.4	-3.06	
R1_10.5	1000	7200.0	94.2	52497.3	52757.8	93.7	51523.6	51756.3	-1.90	93.0	50971.1	51099.8	-3.14	93.0	50895.6	51060.4	-3.22	
R1_10.10	1000	7200.0	93.0	49984.0	50525.7	93.0	49220.4	49360.5	-2.31	92.6	48015.0	48390.5	-4.23	92.7	48454.5	48854.9	-3.31	
R2_10.1	1000	7200.0	26.0	39831.9	40458.1	30.5	37241.1	38080.2	-5.88	32.2	37323.2	37719.2	-6.77	31.2	37407.2	37649.1	-6.94	
R2_10.5	1000	7200.0	21.7	37403.0	37695.6	26.8	34597.7	35281.2	-6.40	25.8	34497.3	35102.8	-6.88	27.6	34422.9	34800.6	-7.68	
R2_10.10	1000	7200.0	20.1	32256.9	32525.9	22.2	31012.4	31171.7	-4.16	23.3	30118.6	30250.6	-7.00	22.7	30109.1	30319.4	-6.78	
RC1_10.1	1000	7200.0	93.6	47760.7	47994.4	92.2	46798.5	47043.7	-1.98	91.5	46285.6	46415.6	-3.29	91.7	46362.2	46639.6	-2.82	
RC1_10.5	1000	7200.0	92.2	47019.3	47412.2	91.6	46257.7	46448.5	-2.03	91.1	45593.0	45718.9	-3.57	91.4	45795.4	45971.7	-3.04	
RC1_10.10	1000	7200.0	90.5	46181.7	46622.4	91.0	45140.7	45367.2	-2.69	90.8	44251.9	44403.5	-4.76	91.0	44627.1	44802.3	-3.90	
RC2_10.1	1000	7200.0	28.7	29458.1	29634.6	29.4	28355.3	28514.0	-3.78	29.5	28324.6	28440.2	-4.03	29.1	28275.9	28349.2	-4.34	
RC2_10.5	1000	7200.0	25.4	26869.9	27242.3	26.0	26111.1	26267.3	-3.54	25.9	25983.3	26076.8	-4.28	25.7	25961.7	26064.3	-4.32	
RC2_10.10	1000	7200.0	19.9	22910.0	23103.9	20.3	22234.7	22409.7	-3.00	19.9	21912.3	21987.3	-4.83	20.1	21885.4	22003.5	-4.76	
MEAN	-	3960.0	37.1	16857.9	16977.3	37.2	16529.0	16625.3	-1.32	37.3	16410.3	16479.4	-1.80	37.3	16423.1	16495.1	-1.80	

Table A7

Comparative results on the 20 *JD* benchmark instances for MA-N, MA-E, MA-NTGA, and MA-ETGA.

Instance	N_C	MA-N				MA-E				MA-NTGA				MA-ETGA						
		M	f^*	f	t	M	f^*	f	t	M	f^*	f	t	M	f^*	f	t			
		Gap(%)	Gap(%)	Gap(%)	Gap(%)	Gap(%)	Gap(%)	Gap(%)	Gap(%)	Gap(%)	Gap(%)	Gap(%)	Gap(%)	Gap(%)	Gap(%)	Gap(%)	Gap(%)	Gap(%)	Gap(%)	
F201	200	41.0	64458.1	64690.3	908.5	41.0	64437.6	64705.0	439.5	0.02	41.0	64297.8	64550.4	424.0	-0.22	41.1	64483.1	64812.3	516.1	0.19
F202	200	42.8	64687.0	64944.5	1089.2	42.9	64848.5	65002.1	376.6	0.09	42.9	64758.0	64875.4	415.1	-0.11	42.8	64698.3	64969.9	608.1	0.04
F203	200	41.2	65667.3	65994.2	1067.7	41.2	65619.3	66042.1	511.8	0.07	41.2	65526.9	65967.3	495.1	-0.04	41.0	65664.1	65854.0	614.9	-0.21
F204	200	41.7	64309.7	64755.8	1164.3	41.6	64461.7	64780.3	442.2	0.04	41.5	64179.1	64629.0							

Table A8

Comparative results on the 100 X benchmark instances for HGS-2012, HGS-CVRP, MA-NTGA, and MA-ETGA.

Instance	N_C	BKS	t	HGS-2012		HGS-CVRP		MA-NTGA		MA-ETGA	
				f^*	Gap(%)	f^*	Gap(%)	f^*	Gap(%)	f^*	Gap(%)
X-n101-k25	100	27591.0	240.0	27591.0	0.00	27591.0	0.00	27591.0	0.00	27591.0	0.00
X-n106-k14	105	26362.0	252.0	26387.0	0.09	26364.0	0.01	26403.0	0.16	26403.0	0.16
X-n110-k13	109	14971.0	261.6	14971.0	0.00	14971.0	0.00	14971.0	0.00	14971.0	0.00
X-n115-k10	114	12747.0	273.6	12747.0	0.00	12747.0	0.00	12747.0	0.00	12747.0	0.00
X-n120-k6	119	13332.0	285.6	13332.0	0.00	13332.0	0.00	13332.0	0.00	13332.0	0.00
X-n125-k30	124	55539.0	297.6	55539.0	0.00	55539.0	0.00	55626.0	0.16	55600.0	0.11
X-n129-k18	128	28940.0	307.2	28940.0	0.00	28940.0	0.00	29012.0	0.25	29020.0	0.28
X-n134-k13	133	10916.0	319.2	10916.0	0.00	10916.0	0.00	10920.0	0.04	10918.0	0.02
X-n139-k10	138	13590.0	331.2	13590.0	0.00	13590.0	0.00	13590.0	0.00	13590.0	0.00
X-n143-k7	142	15700.0	340.8	15700.0	0.00	15700.0	0.00	15726.0	0.17	15740.0	0.25
X-n148-k46	147	43448.0	352.8	43448.0	0.00	43448.0	0.00	43449.0	0.00	43461.0	0.03
X-n153-k22	152	21220.0	364.8	21220.0	0.00	21225.0	0.02	21262.0	0.20	21282.0	0.29
X-n157-k13	156	16876.0	374.4	16876.0	0.00	16876.0	0.00	16876.0	0.00	16876.0	0.00
X-n162-k11	161	14138.0	386.4	14138.0	0.00	14138.0	0.00	14138.0	0.00	14147.0	0.06
X-n167-k10	166	20557.0	398.4	20557.0	0.00	20557.0	0.00	20583.0	0.13	20557.0	0.00
X-n172-k51	171	45607.0	410.4	45607.0	0.00	45607.0	0.00	45610.0	0.01	45616.0	0.02
X-n176-k26	175	47812.0	420.0	47812.0	0.00	47812.0	0.00	47915.0	0.22	47899.0	0.18
X-n181-k23	180	25569.0	432.0	25569.0	0.00	25569.0	0.00	25644.0	0.29	25593.0	0.09
X-n186-k15	185	24145.0	444.0	24145.0	0.00	24145.0	0.00	24154.0	0.04	24180.0	0.14
X-n190-k8	189	16980.0	453.6	16986.0	0.04	16980.0	0.00	17057.0	0.45	17015.0	0.21
X-n195-k51	194	44225.0	465.6	44225.0	0.00	44225.0	0.00	44361.0	0.31	44313.0	0.20
X-n200-k36	199	58578.0	477.6	58578.0	0.00	58578.0	0.00	58730.0	0.26	58711.0	0.23
X-n204-k19	203	19565.0	487.2	19565.0	0.00	19565.0	0.00	19610.0	0.23	19570.0	0.03
X-n209-k16	208	30656.0	499.2	30656.0	0.00	30656.0	0.00	30736.0	0.26	30756.0	0.33
X-n214-k11	213	10856.0	511.2	10856.0	0.00	10856.0	0.00	10927.0	0.65	11005.0	1.37
X-n219-k73	218	117595.0	523.2	117595.0	0.00	117595.0	0.00	117624.0	0.02	117616.0	0.02
X-n223-k34	222	40437.0	532.8	40437.0	0.00	40437.0	0.00	40587.0	0.37	40627.0	0.47
X-n228-k23	227	25742.0	544.8	25742.0	0.00	25742.0	0.00	25870.0	0.50	25881.0	0.54
X-n233-k16	232	19230.0	556.8	19230.0	0.00	19230.0	0.00	19333.0	0.54	19337.0	0.56
X-n237-k14	236	27042.0	566.4	27044.0	0.01	27042.0	0.00	27318.0	1.02	27346.0	1.12
X-n242-k48	241	82751.0	578.4	82771.0	0.02	82771.0	0.02	83443.0	0.84	83319.0	0.69
X-n247-k50	246	37274.0	590.4	37274.0	0.01	37274.0	0.00	37387.0	0.30	37387.0	0.30
X-n251-k28	250	38684.0	600.0	38699.0	0.04	38684.0	0.00	38940.0	0.66	38966.0	0.73
X-n256-k16	255	18839.0	612.0	18880.0	0.22	18839.0	0.00	18920.0	0.43	18929.0	0.48
X-n261-k13	260	26558.0	624.0	26570.0	0.05	26558.0	0.00	26752.0	0.73	26672.0	0.43
X-n266-k58	265	75478.0	636.0	75608.0	0.17	75478.0	0.00	75942.0	0.61	76109.0	0.84
X-n270-k35	269	35291.0	645.6	35303.0	0.03	35303.0	0.03	35525.0	0.66	35543.0	0.71
X-n275-k28	274	21245.0	657.6	21245.0	0.00	21245.0	0.00	21452.0	0.97	21412.0	0.79
X-n280-k17	279	33503.0	669.6	33542.0	0.12	33506.0	0.01	33656.0	0.46	33689.0	0.56
X-n284-k15	283	20215.0	679.2	20225.0	0.05	20231.0	0.08	20632.0	2.06	20724.0	2.52
X-n289-k60	288	95151.0	691.2	95181.0	0.03	95242.0	0.10	96330.0	1.24	96271.0	1.18
X-n294-k50	293	47161.0	703.2	47210.0	0.10	47167.0	0.01	47421.0	0.55	47531.0	0.78
X-n298-k31	297	34231.0	712.8	34231.0	0.00	34231.0	0.00	34416.0	0.54	34552.0	0.94
X-n303-k21	302	21736.0	724.8	21754.0	0.08	21739.0	0.01	21868.0	0.61	21951.0	0.99
X-n308-k13	307	25859.0	736.8	25865.0	0.02	25862.0	0.01	26044.0	0.72	25924.0	0.25
X-n313-k71	312	94043.0	748.8	94050.0	0.01	94045.0	0.00	94891.0	0.90	94800.0	0.80
X-n317-k53	316	78355.0	758.4	78355.0	0.00	78355.0	0.00	78515.0	0.20	78479.0	0.16
X-n322-k28	321	29834.0	770.4	29857.0	0.08	29834.0	0.00	30082.0	0.83	30097.0	0.88
X-n327-k20	326	27532.0	782.4	27576.0	0.16	27532.0	0.00	27738.0	0.75	27850.0	1.16
X-n331-k15	330	31102.0	792.0	31107.0	0.02	31102.0	0.00	31408.0	0.98	31340.0	0.77
X-n336-k84	335	139111.0	804.0	139305.0	0.14	139205.0	0.07	140544.0	1.03	140645.0	1.10
X-n344-k43	343	42050.0	823.2	42067.0	0.04	42061.0	0.03	42468.0	0.99	42509.0	1.09
X-n351-k40	350	25896.0	840.0	25948.0	0.20	25924.0	0.11	26247.0	1.36	26381.0	1.87
X-n359-k29	358	51505.0	859.2	51598.0	0.18	51566.0	0.12	52090.0	1.14	52178.0	1.31
X-n367-k17	366	22814.0	878.4	22814.0	0.00	22814.0	0.00	22986.0	0.75	22902.0	0.39
X-n376-k94	375	147713.0	900.0	147713.0	0.00	147713.0	0.00	147838.0	0.08	147873.0	0.11
X-n384-k52	383	65928.0	919.2	66088.0	0.24	65997.0	0.10	66906.0	1.48	67103.0	1.78
X-n393-k38	392	38260.0	940.8	38260.0	0.00	38260.0	0.00	38596.0	0.88	38620.0	0.94
X-n401-k29	400	66154.0	960.0	66256.0	0.15	66209.0	0.08	66671.0	0.78	66511.0	0.54
X-n411-k19	410	19712.0	984.0	19718.0	0.03	19716.0	0.02	19914.0	1.02	20022.0	1.57
X-n420-k130	419	107798.0	1005.6	107831.0	0.03	107810.0	0.01	108294.0	0.46	108558.0	0.71
X-n429-k61	428	65449.0	1027.2	65524.0	0.11	65484.0	0.05	66112.0	1.01	66286.0	1.28
X-n439-k37	438	36391.0	1051.2	36413.0	0.06	36395.0	0.01	36664.0	0.75	36600.0	0.57
X-n449-k29	448	55233.0	1075.2	55484.0	0.45	55306.0	0.13	56185.0	1.72	56349.0	2.02
X-n459-k26	458	24139.0	1099.2	24182.0	0.18	24139.0	0.00	24467.0	1.36	24395.0	1.06
X-n469-k138	468	221824.0	1123.2	222131.0	0.14	221916.0	0.04	223454.0	0.73	224239.0	1.09
X-n480-k70	479	89449.0	1149.6	89561.0	0.13	89498.0	0.05	90269.0	0.92	90341.0	1.00
X-n491-k59	490	66483.0	1176.0	66653.0	0.26	66569.0	0.13	67578.0	1.65	67629.0	1.72

Table A9

Comparative results on the 100 X benchmark instances for HGS-2012, HGS-CVRP, MA-NTGA, and MA-ETGA (continued).

Instance	N_C	BKS	t	HGS-2012		HGS-CVRP		MA-NTGA		MA-ETGA	
				f^*	Gap(%)	f^*	Gap(%)	f^*	Gap(%)	f^*	Gap(%)
X-n502-k39	501	69226.0	1202.4	69264.0	0.05	69230.0	0.01	69566.0	0.49	69564.0	0.49
X-n513-k21	512	24201.0	1228.8	24201.0	0.00	24201.0	0.00	24429.0	0.94	24509.0	1.27
X-n524-k153	523	154593.0	1255.2	154713.0	0.08	154646.0	0.03	154764.0	0.11	155331.0	0.48
X-n536-k96	535	94846.0	1284.0	95125.0	0.29	95040.0	0.20	95622.0	0.82	96355.0	1.59
X-n548-k50	547	86700.0	1312.8	86888.0	0.22	86710.0	0.01	87426.0	0.84	87699.0	1.15
X-n561-k42	560	42717.0	1344.0	42738.0	0.05	42726.0	0.02	43317.0	1.40	43388.0	1.57
X-n573-k30	572	50673.0	1372.8	50797.0	0.24	50757.0	0.17	51461.0	1.56	51379.0	1.39
X-n586-k159	585	190316.0	1404.0	190576.0	0.14	190470.0	0.08	191836.0	0.80	192258.0	1.02
X-n599-k92	598	108451.0	1435.2	108712.0	0.24	108605.0	0.14	110447.0	1.84	110534.0	1.92
X-n613-k62	612	59535.0	1468.8	59698.0	0.27	59636.0	0.17	60571.0	1.74	60687.0	1.93
X-n627-k43	626	62164.0	1502.4	62377.0	0.34	62238.0	0.12	63015.0	1.37	63096.0	1.50
X-n641-k35	640	63682.0	1536.0	63976.0	0.46	63782.0	0.16	64516.0	1.31	64684.0	1.57
X-n655-k131	654	106780.0	1569.6	106841.0	0.06	106785.0	0.00	107248.0	0.44	107269.0	0.46
X-n670-k130	669	146332.0	1605.6	146833.0	0.34	146640.0	0.21	147491.0	0.79	147803.0	1.01
X-n685-k75	684	68205.0	1641.6	68414.0	0.31	68288.0	0.12	69319.0	1.63	69510.0	1.91
X-n701-k44	700	81923.0	1680.0	82302.0	0.46	82075.0	0.19	83308.0	1.69	83523.0	1.95
X-n716-k35	715	43373.0	1716.0	43541.0	0.39	43459.0	0.20	44188.0	1.88	44119.0	1.72
X-n733-k159	732	136187.0	1756.8	136405.0	0.16	136323.0	0.10	137896.0	1.25	138426.0	1.64
X-n749-k98	748	77269.0	1795.2	77671.0	0.52	77563.0	0.38	78836.0	2.03	78970.0	2.20
X-n766-k71	765	114417.0	1836.0	114834.0	0.36	114679.0	0.23	117135.0	2.38	116629.0	1.93
X-n783-k48	782	72386.0	1876.8	72797.0	0.57	72704.0	0.44	73679.0	1.79	73718.0	1.84
X-n801-k40	800	73305.0	1920.0	73678.0	0.51	73396.0	0.12	74533.0	1.68	74639.0	1.82
X-n819-k171	818	158121.0	1963.2	158639.0	0.33	158391.0	0.17	159878.0	1.11	161000.0	1.82
X-n837-k142	836	193737.0	2006.4	194444.0	0.36	194103.0	0.19	196109.0	1.22	196834.0	1.60
X-n856-k95	855	88965.0	2052.0	89110.0	0.16	88986.0	0.02	89939.0	1.09	90023.0	1.19
X-n876-k59	875	99299.0	2100.0	99765.0	0.47	99596.0	0.30	100718.0	1.43	100931.0	1.64
X-n895-k37	894	53860.0	2145.6	54134.0	0.51	54023.0	0.30	55170.0	2.43	55189.0	2.47
X-n916-k207	915	329179.0	2196.0	329918.0	0.22	329572.0	0.12	332728.0	1.08	334515.0	1.62
X-n936-k151	935	132715.0	2244.0	133102.0	0.29	133121.0	0.31	134944.0	1.68	135026.0	1.74
X-n957-k87	956	85465.0	2294.4	85709.0	0.29	85506.0	0.05	86748.0	1.50	86780.0	1.54
X-n979-k58	978	118976.0	2347.2	119353.0	0.32	119180.0	0.17	120156.0	0.99	120106.0	0.95
X-n1001-k43	1000	72355.0	2400.0	72824.0	0.65	72678.0	0.45	74271.0	2.65	74212.0	2.57
MEAN	-	63106.7	989.3	63222.3	0.13	63166.6	0.06	63716.1	0.83	63810.9	0.92

Table A10

Comparative results on the 90 GH benchmark instances for DIMACS, HGS-DIMACS, MA-NTGA, and MA-ETGA.

Instance	N_C	BKS	t	DIMACS		HGS-DIMACS		MA-NTGA		MA-ETGA	
				f^*	Gap(%)	f^*	Gap(%)	f^*	Gap(%)	f^*	Gap(%)
C1.2.1	200	2698.6	1800.0	2698.6	0.00	2698.6	0.00	2698.6	0.00	2698.6	0.00
C1.2.5	200	2694.9	1800.0	2694.9	0.00	2694.9	0.00	2694.9	0.00	2694.9	0.00
C1.2.10	200	2624.7	1800.0	2624.7	0.00	2624.7	0.00	2624.7	0.00	2624.7	0.00
C2.2.1	200	1922.1	1800.0	1922.1	0.00	1922.1	0.00	1922.1	0.00	1922.1	0.00
C2.2.5	200	1869.6	1800.0	1869.6	0.00	1869.6	0.00	1869.6	0.00	1869.6	0.00
C2.2.10	200	1791.2	1800.0	1791.2	0.00	1791.2	0.00	1791.2	0.00	1791.2	0.00
R1.2.1	200	4667.2	1800.0	4667.2	0.00	4667.2	0.00	4667.2	0.00	4667.2	0.00
R1.2.5	200	4053.2	1800.0	4053.2	0.00	4053.2	0.00	4053.2	0.00	4053.2	0.00
R1.2.10	200	3293.1	1800.0	3293.1	0.00	3293.1	0.00	3293.1	0.00	3293.8	0.02
R2.2.1	200	3468.0	1800.0	3468.0	0.00	3468.0	0.00	3507.5	1.14	3478.4	0.30
R2.2.5	200	3061.1	1800.0	3061.1	0.00	3063.8	0.09	3069.1	0.26	3063.6	0.08
R2.2.10	200	2549.4	1800.0	2549.4	0.00	2549.4	0.00	2557.8	0.33	2556.1	0.26
RC1.2.1	200	3516.9	1800.0	3516.9	0.00	3516.9	0.00	3516.9	0.00	3516.9	0.00
RC1.2.5	200	3325.6	1800.0	3325.6	0.00	3325.6	0.00	3325.6	0.00	3326.3	0.02
RC1.2.10	200	2990.5	1800.0	2990.5	0.00	2994.9	0.15	2993.8	0.11	2996.9	0.21
RC2.2.1	200	2797.4	1800.0	2797.4	0.00	2797.4	0.00	2797.4	0.00	2797.4	0.00
RC2.2.5	200	2491.4	1800.0	2491.4	0.00	2491.4	0.00	2491.4	0.00	2492.1	0.03
RC2.2.10	200	1989.2	1800.0	1989.2	0.00	1989.2	0.00	2000.0	0.54	1997.0	0.39
C1.4.1	400	7138.8	3600.0	7138.8	0.00	7138.8	0.00	7138.8	0.00	7138.8	0.00
C1.4.5	400	7138.8	3600.0	7138.8	0.00	7138.8	0.00	7138.8	0.00	7138.8	0.00
C1.4.10	400	6825.4	3600.0	6825.4	0.00	6825.4	0.00	6825.7	0.00	6826.5	0.02
C2.4.1	400	4100.3	3600.0	4100.3	0.00	4100.3	0.00	4100.3	0.00	4100.3	0.00
C2.4.5	400	3923.2	3600.0	3923.2	0.00	3923.2	0.00	3927.5	0.11	3923.2	0.00
C2.4.10	400	3665.1	3600.0	3665.1	0.00	3665.1	0.00	3665.1	0.00	3665.1	0.00

Table A11

Comparative results on the 90 *GH* benchmark instances for DIMACS, HGS-DIMACS, MA-NTGA, and MA-ETGA (continued).

Instance	N_C	BKS	t	DIMACS		HGS-DIMACS		MA-NTGA		MA-ETGA	
				f^*	Gap(%)	f^*	Gap(%)	f^*	Gap(%)	f^*	Gap(%)
R1.4.1	400	10305.8	3600.0	10305.8	0.00	10305.8	0.00	10313.8	0.08	10337.6	0.31
R1.4.5	400	9184.6	3600.0	9188.6	0.04	9190.3	0.06	9208.7	0.26	9198.4	0.15
R1.4.10	400	8077.8	3600.0	8086.4	0.11	8081.9	0.05	8109.5	0.39	8138.7	0.75
R2.4.1	400	7520.7	3600.0	7520.7	0.00	7520.7	0.00	7559.7	0.52	7526.8	0.08
R2.4.5	400	6567.9	3600.0	6567.9	0.00	6567.9	0.00	6568.1	0.00	6577.1	0.14
R2.4.10	400	5638.1	3600.0	5645.9	0.14	5657.7	0.35	5690.2	0.92	5694.0	0.99
RC1.4.1	400	8522.9	3600.0	8524.0	0.01	8524.0	0.01	8524.0	0.01	8527.2	0.05
RC1.4.5	400	8152.3	3600.0	8172.4	0.25	8154.6	0.03	8196.4	0.54	8206.7	0.67
RC1.4.10	400	7581.2	3600.0	7585.3	0.05	7589.0	0.10	7634.5	0.70	7634.0	0.70
RC2.4.1	400	6147.3	3600.0	6147.3	0.00	6147.3	0.00	6156.2	0.14	6148.7	0.02
RC2.4.5	400	5392.3	3600.0	5396.9	0.09	5392.3	0.00	5400.1	0.14	5394.7	0.04
RC2.4.10	400	4252.3	3600.0	4252.3	0.00	4252.3	0.00	4266.6	0.34	4261.6	0.22
C1.6.1	600	14076.6	3600.0	14076.6	0.00	14076.6	0.00	14076.6	0.00	14076.6	0.00
C1.6.5	600	14066.8	3600.0	14066.8	0.00	14066.8	0.00	14066.8	0.00	14066.8	0.00
C1.6.10	600	13617.5	3600.0	13636.5	0.14	13636.6	0.14	13626.3	0.06	13640.1	0.17
C2.6.1	600	7752.2	3600.0	7752.2	0.00	7752.2	0.00	7752.2	0.00	7752.2	0.00
C2.6.5	600	7553.8	3600.0	7553.8	0.00	7553.8	0.00	7553.8	0.00	7553.8	0.00
C2.6.10	600	7123.9	3600.0	7123.9	0.00	7128.0	0.06	7131.5	0.11	7136.0	0.17
R1.6.1	600	21274.2	3600.0	21274.2	0.00	21312.5	0.18	21314.5	0.19	21315.5	0.19
R1.6.5	600	19294.9	3600.0	19305.7	0.06	19322.6	0.14	19435.8	0.73	19463.8	0.88
R1.6.10	600	17583.7	3600.0	17648.1	0.37	17603.2	0.11	17711.0	0.72	17795.1	1.20
R2.6.1	600	15145.3	3600.0	15145.3	0.00	15145.3	0.00	15274.1	0.85	15194.9	0.33
R2.6.5	600	13790.2	3600.0	13809.7	0.14	13803.7	0.10	13895.0	0.76	13926.5	0.99
R2.6.10	600	11837.0	3600.0	11851.6	0.12	11852.9	0.13	12010.4	1.46	11988.6	1.28
RC1.6.1	600	16944.2	3600.0	16981.3	0.22	16961.1	0.10	17037.9	0.55	17069.3	0.74
RC1.6.5	600	16536.3	3600.0	16580.4	0.27	16597.4	0.37	16682.9	0.89	16696.2	0.97
RC1.6.10	600	15651.3	3600.0	15672.8	0.14	15737.1	0.55	15870.0	1.40	15915.0	1.68
RC2.6.1	600	11966.1	3600.0	11979.3	0.11	11966.1	0.00	12005.7	0.33	11986.7	0.17
RC2.6.5	600	11080.7	3600.0	11082.5	0.02	11080.7	0.00	11111.9	0.28	11109.5	0.26
RC2.6.10	600	8973.3	3600.0	9014.8	0.46	8976.1	0.03	9028.3	0.61	9036.1	0.70
C1.8.1	800	25156.9	3600.0	25156.9	0.00	25156.9	0.00	25156.9	0.00	25156.9	0.00
C1.8.5	800	25138.6	3600.0	25138.6	0.00	25138.6	0.00	25138.6	0.00	25138.6	0.00
C1.8.10	800	24026.7	3600.0	24030.4	0.02	24046.3	0.08	24094.3	0.28	24091.5	0.27
C2.8.1	800	11631.9	3600.0	11631.9	0.00	11632.7	0.01	11631.9	0.00	11631.9	0.00
C2.8.5	800	11395.6	3600.0	11395.6	0.00	11395.6	0.00	11395.6	0.00	11395.6	0.00
C2.8.10	800	10946.0	3600.0	10946.0	0.00	10946.7	0.01	10950.2	0.04	10957.6	0.11
R1.8.1	800	36345.0	3600.0	36393.3	0.13	36465.0	0.33	36641.8	0.82	36704.2	0.99
R1.8.5	800	33494.0	3600.0	33640.0	0.44	33658.8	0.49	33815.4	0.96	33849.3	1.06
R1.8.10	800	30918.3	3600.0	31059.8	0.46	31138.4	0.71	31436.6	1.68	31573.6	2.12
R2.8.1	800	24963.8	3600.0	24986.8	0.09	24998.9	0.14	25237.3	1.10	25129.0	0.66
R2.8.5	800	22795.6	3600.0	22802.0	0.03	22808.2	0.06	23026.9	1.01	22929.3	0.59
R2.8.10	800	19964.2	3600.0	20016.5	0.26	20007.8	0.22	20154.0	0.95	20230.8	1.34
RC1.8.1	800	29952.8	3600.0	30039.5	0.29	30058.9	0.35	30186.5	0.78	30193.5	0.80
RC1.8.5	800	29219.9	3600.0	29306.4	0.30	29327.6	0.37	29514.3	1.01	29556.2	1.15
RC1.8.10	800	28168.5	3600.0	28210.7	0.15	28283.1	0.41	28564.8	1.41	28786.5	2.19
RC2.8.1	800	19201.3	3600.0	19213.2	0.06	19213.4	0.06	19279.2	0.41	19239.5	0.20
RC2.8.5	800	17466.1	3600.0	17493.3	0.16	17466.1	0.00	17540.8	0.43	17595.1	0.74
RC2.8.10	800	14370.9	3600.0	14445.3	0.52	14376.2	0.04	14470.6	0.69	14478.0	0.75
C1.10.1	1000	42444.8	7200.0	42444.8	0.00	42444.8	0.00	42444.8	0.00	42444.8	0.00
C1.10.5	1000	42434.8	7200.0	42434.8	0.00	42434.8	0.00	42434.8	0.00	42435.5	0.00
C1.10.10	1000	39816.8	7200.0	39874.5	0.14	40149.5	0.84	40030.1	0.54	40056.8	0.60
C2.10.1	1000	16841.1	7200.0	16841.1	0.00	16841.1	0.00	16841.1	0.00	16841.1	0.00
C2.10.5	1000	16521.3	7200.0	16521.3	0.00	16521.3	0.00	16521.9	0.00	16522.9	0.01
C2.10.10	1000	15728.6	7200.0	15728.6	0.00	15728.6	0.00	15773.0	0.28	15750.8	0.14
R1.10.1	1000	53026.1	7200.0	53233.9	0.39	53341.7	0.60	53488.9	0.87	53522.0	0.94
R1.10.5	1000	50406.7	7200.0	50487.8	0.16	50596.5	0.38	50971.1	1.12	50895.6	0.97
R1.10.10	1000	47364.6	7200.0	47570.6	0.43	47690.5	0.69	48015.0	1.37	48454.5	2.30
R2.10.1	1000	36881.0	7200.0	36899.4	0.05	36891.3	0.03	37323.2	1.20	37079.2	0.54
R2.10.5	1000	34132.8	7200.0	34233.0	0.29	34195.3	0.18	34497.3	1.07	34422.9	0.85
R2.10.10	1000	29840.5	7200.0	29956.9	0.39	29882.3	0.14	30118.6	0.93	30109.1	0.90
RC1.10.1	1000	45790.7	7200.0	45948.5	0.34	46047.3	0.56	46285.6	1.08	46362.2	1.25
RC1.10.5	1000	45028.1	7200.0	45235.5	0.46	45349.6	0.71	45593.0	1.25	45795.4	1.70
RC1.10.10	1000	43533.7	7200.0	43745.6	0.49	43635.1	0.23	44251.9	1.65	44627.1	2.51
RC2.10.1	1000	28122.6	7200.0	28190.8	0.24	28192.1	0.25	28324.6	0.72	28275.9	0.55
RC2.10.5	1000	25797.5	7200.0	25892.3	0.37	25862.2	0.25	25983.3	0.72	25961.7	0.64
RC2.10.10	1000	21731.2	7200.0	21848.3	0.54	21862.3	0.60	21912.3	0.83	21885.4	0.71
MEAN	-	16297.8	3960.0	16328.2	0.11	16337.2	0.13	16410.3	0.45	16423.1	0.48

Table A12
Comparative results on the 20 *JD* benchmark instances for MA-FIRD, MA-NTGA,
and MA-ETGA.

Instance	N_C	BKS	MA-FIRD			MA-NTGA			MA-ETGA		
			f^*	t	Gap(%)	f^*	t	Gap(%)	f^*	t	Gap(%)
F201	200	64083.4	64083.4	1360.4	0.00	64297.8	424.0	0.33	64483.1	516.1	0.62
F202	200	64378.1	64378.1	1236.1	0.00	64758.0	415.1	0.59	64698.3	608.1	0.50
F203	200	65547.4	65547.4	1349.0	0.00	65526.9	495.1	-0.03	65664.1	614.9	0.18
F204	200	64037.3	64037.3	1429.9	0.00	64179.1	532.0	0.22	64310.7	641.4	0.43
F401	400	115876.0	115876.0	7005.8	0.00	116999.0	841.8	0.97	117057.0	1056.2	1.02
F402	400	121997.0	121997.0	7082.8	0.00	122429.0	865.5	0.35	122369.0	1567.1	0.30
F403	400	115540.0	115540.0	6729.3	0.00	115920.0	874.3	0.33	116693.0	1109.8	1.00
F404	400	119451.0	119451.0	7129.2	0.00	119242.0	882.7	-0.17	119777.0	1456.1	0.27
F601	600	174108.0	174108.0	7203.1	0.00	173141.0	1731.3	-0.56	173896.0	1571.3	-0.12
F602	600	178317.0	178317.0	7202.7	0.00	177893.0	1503.2	-0.24	179052.0	1836.8	0.41
F603	600	177979.0	177979.0	7202.7	0.00	177320.0	1378.0	-0.37	177997.0	1567.1	0.01
F604	600	178201.0	178201.0	7202.8	0.00	176527.0	1651.1	-0.94	177806.0	1712.8	-0.22
F801	800	208325.0	208325.0	7208.8	0.00	205657.0	2362.7	-1.28	207300.0	2589.9	-0.49
F802	800	206214.0	206214.0	7207.2	0.00	204164.0	2302.7	-0.99	205251.0	2696.9	-0.47
F803	800	210213.0	210213.0	7207.6	0.00	207664.0	2167.3	-1.21	207585.0	2737.8	-1.25
F804	800	203971.0	203971.0	7206.4	0.00	202271.0	2165.4	-0.83	203116.0	2546.4	-0.42
F1001	1000	303113.0	303113.0	7218.1	0.00	297090.0	4617.2	-1.99	297325.0	3434.4	-1.91
F1002	1000	299833.0	299833.0	7216.6	0.00	292779.0	4010.4	-2.35	294712.0	3511.3	-1.71
F1003	1000	301051.0	301051.0	7211.7	0.00	292581.0	4556.9	-2.81	294946.0	3187.9	-2.03
F1004	1000	298555.0	298555.0	7219.0	0.00	292222.0	4875.1	-2.12	293905.0	3223.3	-1.56
MEAN	-	173539.5	173539.5	5991.5	0.00	171633.0	1932.6	-0.66	172397.2	1909.3	-0.27